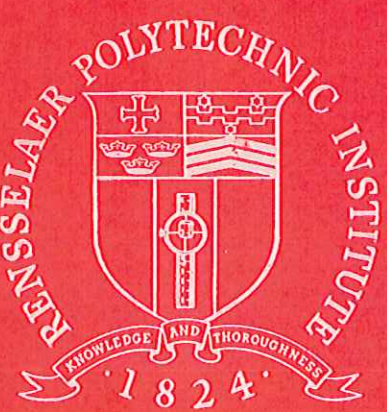


HIGH ENERGY ELECTRON IMPACT
IONIZATION



Rensselaer Polytechnic Institute
Troy, New York 12181

HIGH ENERGY ELECTRON IMPACT
IONIZATION

Application to Elemental Analysis by
Energy Dispersive X-Ray Spectrometry

and

K-Shell Ionization Cross Sections at 2 MeV

HIGH ENERGY ELECTRON IMPACT
IONIZATION

by

Ronald P. Collé

A Thesis Submitted to the Graduate
Faculty of Rensselaer Polytechnic Institute
in Partial Fulfillment of the
Requirements for the Degree of
DOCTOR OF PHILOSOPHY
Major Subject: Chemistry

Approved by the
Examining Committee:

Ivor L. Preiss
Ivor L. Preiss, Thesis Advisor

David A. Aikens
David A. Aikens, Member

Herbert M. Clark
Herbert M. Clark, Member

Heinrich A. Medicus
Heinrich A. Medicus, Member

Kenneth J. Miller
Kenneth J. Miller, Member

Rensselaer Polytechnic Institute
Troy, New York

June 1972
(For Graduation September, 1972)

CONTENTS

	Page
TABLE OF CONTENTS	iii
LIST OF FIGURES	v
LIST OF TABLES	vii
ACKNOWLEDGEMENT	ix
ABSTRACT	xi
1. INTRODUCTION	1
1.1 Electron Impact Ionization	2
1.1.1 General	2
1.1.2 K-Shell Ionization Cross Sections	8
1.1.3 K-Shell Fluorescence Yields	19
1.1.4 K-Shell Radiative Transition Probability Ratios	25
1.2 Application to Elemental Analyses	26
2. EXPERIMENTAL	34
2.1 SUNY/Albany Dynamitron	34
2.1.1 Electron Energy Calibration	34
2.1.2 Electron Beam Positioning	38
2.2 Sample and Target Preparations	45
2.2.1 General Targeting Procedures	45
2.2.2 Samples, Sample Solutions and Targets	46
a) References	46
b) NBS Metal Alloy Standards	61
c) Others	62
2.2.3 Target Composition and Evaluation of Solution Sampling Technique	67
2.3 X-Ray Spectrometers and Detection Configuration	74
2.3.1 Systems A and B: Si(Li)	75
2.3.2 System C: Ge(Li)	76
2.3.3 System D: Si(Li) - Vacuum Coupled	78

CONTENTS (continued)

	Page
2.4 Measurement Procedures and Data Analysis	80
2.4.1 Relative X-Ray Yields	84
2.4.2 Elemental Analysis	86
3. RESULTS AND DISCUSSION	89
3.1 Relative X-Ray Yields and Elemental Analysis	89
3.2 Relative K-Shell Ionization Cross Sections	119
4. CONCLUSIONS	135
4.1 Application to Elemental Analysis	135
4.2 K-Shell Ionization Cross Sections	137
5. LITERATURE CITED	140
6. APPENDICES	145
6.1 Appendix A: Silicon X-Ray Escape Peak Correction for Analysis of Iron in Presence of Copper	146
6.2 Appendix B: Transmission Measurements for Target Self-Absorption Corrections	150
6.3 Appendix C: Chemical Assay of CdCl ₂ ·2½H ₂ O Reference Sample Reagent	157
6.4 Appendix D: Calculation of Relative Intrinsic Detection Efficiencies for Si(Li) and Ge(Li) Detectors	159

LIST OF FIGURES

	Page
Figure 1.1 Theoretical Cross Section Parameter (S) as a Function of the Ratio of the Electron Kinetic Energy (E) to the K-Shell Ionization Energy (I_K)	11
Figure 1.2 Theoretical K-Shell Ionization Cross Section (σ_K) as a Function of Electron Energy for Aluminum, Nickel, Tin and Gold	20
Figure 1.3 Theoretical K-Shell Ionization Cross Section (σ_K) as a Function of Atomic Number (Z) for 2 MeV Electrons	21
Figure 1.4 Theoretical K-Shell Fluorescence Yields (ω_K) as a Function of Atomic Number (Z)	23
Figure 1.5 Theoretical and Experimental K-Shell Fluorescence Yields (ω_K) as a Function of Atomic Number (Z)	24
Figure 1.6 Theoretical and Experimental Transition Probability Ratios ($K\beta/K\alpha$) as a Function of Atomic Number (Z)	27
Figure 1.7 $K\alpha$ X-Ray Production [$\sigma_K \omega_K / (1 + K\beta/K\alpha)$] as a Function of Atomic Number (Z) for Ionization by 2 MeV Electrons	30
Figure 2.1 Physical Arrangement of SUNY/Albany Dynamitron Accelerator Beam Lines	35
Figure 2.2 Electron Bremsstrahlung Radiator Assembly	37
Figure 2.3 Dynamitron Energy Calibration by $^9\text{Be}(\gamma, n)$ Reaction Threshold	39
Figure 2.4 Dynamitron Zero-Degree Beam Line Sections	40
Figure 2.5 Target Chamber Assembly	42
Figure 2.6 Aluminum Target Frame Detail	43
Figure 2.7 Removable Aperture Assembly	44
Figure 2.8 Physical Arrangement for System B	77

LIST OF FIGURES (continued)

	Page
Figure 2.9 Physical Arrangement for System C	79
Figure 2.10 Physical Arrangement for System D	81
Figure 3.1 Relative K X-Ray Yields ($Y_{K\alpha}$ and $Y_{K\beta}$) as a Function of Atomic Number (Z) for Systems B, C and D	95
Figure 3.2 Typical X-Ray Spectra of the Reference Samples Obtained with the Si(Li) Detector (System D)	100
Figure 3.3 Typical X-Ray Spectra of the Reference Samples Obtained with the Ge(Li) Detector (System C)	101
Figure 3.4 Typical Low Energy X-Ray Spectra Obtained with the Si(Li) Detector (System D)	108
Figure 3.5 X-Ray Spectra of the Phosphor Bronze Bearing Metal (NBS No. 63)	112
Figure 3.6 X-Ray Spectra of the Cast Bronze (NBS No. 52) Obtained with the Si(Li) Detector (System C)	115
Figure 3.7 Experimental and Theoretical Relative K-Shell Ionization Cross Sections [$\sigma_K(Z)/\sigma_K(Cd)$] as a Function of Atomic Number (Z) for 2 MeV Electrons	131
Figure A.1 X-Ray Spectrum of Cu K X-Rays Obtained with a Si(Li) Detector Showing the Si K X-Ray Escape Peak	149
Figure B.1 Fractional Target Transmission (T) of $K\alpha$ X-Rays for Element Z from the Z/Cd Lens Tissue Reference Targets as a Function of Atomic Number (Z)	156

LIST OF TABLES

	Page
Table 1.1 Comparison of Experimental and Theoretical K-Shell Ionization Cross Sections (σ_K) for Relativistic Electrons with Energy (E), 0.5 MeV \leq E \leq 10 MeV	16
Table 2.1 Sample Solutions and Preparation for Filter Paper Targets	48
Table 2.2 Sample Solutions and Preparation for Lens Tissue Targets	51
Table 2.3 Reference Sample Reagents	55
Table 2.4 Assay for NBS Standard No. 52	63
Table 2.5 Assay for NBS Standard No. 54	64
Table 2.6 Assay for NBS Standard No. 63	65
Table 2.7 Sample Solutions for Target Preparation of NBS Standards	66
Table 2.8 Composition of Cu/Cd Lens Tissue Targets	69
Table 2.9 Composition of Pb/Cd Lens Tissue Targets	70
Table 2.10 Sample Thickness for Lens Tissue Targets	72
Table 3.1 Relative K X-Ray Yields for System B	91
Table 3.2 Relative K X-Ray Yields for System C	92
Table 3.3 Relative K X-Ray Yields for System D	93
Table 3.4 Results of Weight Ratios with Respect to Sn for the NBS Metal Alloy Standards	111
Table 3.5 Results of Weight Ratios with Respect to Cu for the NBS Metal Alloy Standards	114
Table 3.6 Results of Weight Ratios with Respect to the Total Sample for the NBS Metal Alloy Standards . .	118
Table 3.7 Tabulation of Values for $\omega_K(Z)/\omega_K(Cd)$, $[1 + K\beta/K\alpha(Z)]/[1 + K\beta/K\alpha(Cd)]$, $T_{K\alpha}(Z)/T_{K\alpha}(Cd)$ and $A_{K\alpha}(Z)/A_{K\alpha}(Cd)$	122

LIST OF TABLES (continued)

	Page
Table 3.8 Relative Intrinsic Detection Efficiencies [$\epsilon_{K\alpha}(Z)/\epsilon_{K\alpha}(Cd)$] of the Ge(Li) and Si(Li) Detectors for K α X-Rays	124
Table 3.9 Comparison of Experimental and Theoretical Relative K-Shell Ionization Cross Sections [$\sigma_K(Z)/\sigma_K(Cd)$] for 2 MeV Electrons	130
Table 3.10 Comparison of Experimental and Theoretical K-Shell Ionization Cross Sections for 2 MeV Electrons	133
Table B.1 Transmission Measurements on Reference Sample Lens Tissue Targets	154
Table B.2 Transmission Measurements on NBS Metal Alloy Sample Lens Tissue Targets	155

ACKNOWLEDGEMENT

The author is grateful to his many teachers, not only for their imparted knowledge, but also for their generous friendship. In particular, thanks are due Dr. Ivor L. Preiss, for the never ending enthusiasm and generous support, and for providing the environment and freedom necessary to satisfy scientific curiosity; to Dr. Herbert M. Clark, for being the authors constant source of information and inspiration; to Drs. Wilfried Scholz and Hassa Bakhru, for letting a chemist do physics with them; and especially to Dr. Angela Li-Scholz, who patiently attempted to instill scientific maturity through endless hours of conversation and "gedenken" experiments.

The U. S. Atomic Energy Commission [Contract Number AT(11-1)-3964, old AT(30-1)-3948] and the Office of Naval Research [Project THEMIS Contract Number N00014-68-A-0495] is gratefully acknowledged for subsidizing his graduate education. This work, conducted at the Nuclear Accelerator Laboratory of the State University of New York at Albany, would not have been possible without the efforts of the Director, Dr. Jagadish B. Garg, and Art Haberl and Chris Wrzenski of the technical staff. Their cooperation, helpfullness and competance is deeply appreciated. The hospitality extended by the Physics Department at SUNY/Albany in the course of this work is also appreciated.

The author would also like to express his appreciation to Dr. Preiss for being his thesis advisor, and to Drs. Clark, Aikens, Medicus and Miller for serving on his doctoral committee. Their many suggestions and valuable criticisms were most welcome. Thanks are also due Dr.

Donald S. Miller for his assistance in making the atomic absorption analyses, Dr. Clark for providing the NBS standards and other needed supplies, Drs. Walter Bambynek, Bernd Crasemann, R. W. Fink, et. al. for providing their prepublication compilation of fluorescence yields, Mr. Jack LaBrecque for procuring some of the needed chemicals, Ms. Bonnie Hosgood for the efficient and expedient typing of this thesis, Dick Cavett for companionship in the dark hours during all phases of this work, and extend a special thanks to Drs. Li-Scholz and Scholz for making this thesis a reality.

Lastly, the author wishes to thank his wife, Judith, to whom he is indebted for her charity, perseverance, understanding and self-sacrifice in creating the ideal atmosphere to do chemistry. To her, this thesis is dedicated.

R. Collé
June, 1972

ABSTRACT

A method has been demonstrated in which the emission of characteristic X-rays following impact ionization by electrons of several MeV energy is used for elemental analysis by energy dispersive X-ray spectrometry. Because of the unique properties of MeV electrons with respect to their X-ray production yield and range in solids, the method has comparable sensitivity over a wide range of elements and does not require stringent sample preparation techniques. By using energy dispersive analysis to detect the X-rays, a simultaneous determination of the weight fraction of the elements in an unknown sample is possible from a procedure based entirely on empirically determined relative X-ray yields.

The relative X-ray yields were established from simultaneous measurements of the X-rays from targets containing a known ratio of two elements. The targets were made by dissolving solid samples and adsorbing the solutions onto identical thin adsorbent supporting matrices of either filter paper (8.15 mg/cm^2) or lens tissue (1.35 mg/cm^2). The thinner lens tissue targets were found to be more advantageous in several respects and were therefore used in the majority of the work. Typically, these latter targets contained $\sim 1 \text{ mg/cm}^2$ of sample material. Various detection systems using high resolution liquid nitrogen cooled Ge(Li) and Si(Li) detectors were employed for the studies. For one of the detection systems utilized, the Si(Li) detector was directly vacuum coupled to the evacuated electron beam tube. In this case, it was possible to detect all elements down to aluminum ($Z = 13$). The method

developed for measuring the relative yields and making the elemental assays was shown to be both simple and rapid. The entire procedure requires only relative measurements. All of the measured quantities are obtained from ratios of simultaneously recorded X-ray intensities and weight ratios. It, therefore, does not require any absolute measurements of the number of atoms or the number of X-rays produced.

The capability of the method for quantitative analysis was tested by analyzing three standard metal alloy samples obtained from the National Bureau of Standards. Elements ranging from iron ($Z = 26$) to lead ($Z = 82$) with concentrations from 0.06% to 88% were quantitatively determined. In general, good approximate agreement with the reported assays was found. For even the minor constituents, the accuracy of the results were of the order of 5-10%.

Relative cross sections for K-shell ionization by 2.04 ± 0.01 MeV electrons for 31 elements were extracted from the relative $K\alpha$ X-ray yield measurements. The measurements were made with the Si(Li) detector for 27 of the elements in the range $Z = 23 - 70$, and with the Ge(Li) detector for 14 of the elements in the range $Z = 35 - 83$. In the cases when comparisons were possible, the two sets of measurements were in good agreement. The results were compared to the Kolbenstvedt* theory for K-shell ionization by relativistic electrons. In general, the theoretical values were found to be in good approximate agreement ($\pm 25\%$) with the measurements. In the medium Z region ($Z \approx 50$), the agreement is excellent, but systematic deviations were found in both low and high Z regions. The cross sections predicted by the Kolbenstvedt theory are systematically too small in the low Z region ($Z \lesssim 40$) and too large in

the high Z region ($Z \gtrsim 60$). The deviation of the Kolbenstvedt theory in the heavy elements was observed in prior measurements for gold ($Z = 79$) at 2 MeV[†] and also at 2.5 and 7.1 MeV.[‡]

The relative cross sections were combined with the absolute cross section measurement of Rester and Dance[†] for tin at 2 MeV [$\sigma_K(\text{Sn}) = 44 \pm 4 \text{ b}$] to obtain absolute cross sections for all 31 elements. They are (in barns): V, 361 ± 53 ; Cr, 277 ± 41 ; Mn, 276 ± 43 ; Fe, 261 ± 38 ; Co, 246 ± 40 ; Ni, 240 ± 38 ; Cu, 203 ± 30 ; Zn, 188 ± 30 ; As, 138 ± 21 ; Se, 114 ± 19 ; Br, 111 ± 12 ; Rb, 105 ± 15 ; Sr, 91.2 ± 13.1 ; Ag, 57.8 ± 5.2 ; Cd, 46.8 ± 4.1 ; In, 44.2 ± 4.0 ; Sb, 42.1 ± 3.7 ; Te, 38.6 ± 3.4 ; Ba, 30.9 ± 2.8 ; La, 19.2 ± 2.5 ; Ce, 23.6 ± 3.1 ; Pr, 24.1 ± 3.2 ; Nd, 22.0 ± 2.0 ; Sm, 21.1 ± 2.0 ; Eu, 21.5 ± 3.1 ; Gd, 21.2 ± 2.0 ; Er, 16.9 ± 1.6 ; Yb, 15.6 ± 1.6 ; Pt, 11.9 ± 1.5 ; Pb, 10.0 ± 1.2 ; Bi, 9.5 ± 1.2 .

*H. Kolbenstvedt, J. Appl. Phys. 38, 4785 (1967).

†D. H. Rester and W. E. Dance, Phys. Rev. 152, 1 (1966).

‡K. H. Berkner, S. N. Kaplan and R. V. Pyle, Bull. Amer. Phys. Soc. 15, 786 (1970).

Part 1

INTRODUCTION

Although the accumulated knowledge in the last sixty years of atomic structure and processes is overwhelmingly impressive, the entire subject of inner shell ionization of atoms by electron impact at several MeV energy has been rather neglected. This is evidenced by both the lack of adequate theoretical calculations for the electron atom collision and the sparsity of cross section measurements at these energies. Only a single theoretical calculation for K-shell ionization cross sections exists which is valid for the entire periodic range of elements and for electron energies from 100 to 1000 times the K-shell ionization energy. Similarly, experimental cross sections have been obtained for only seven elements in the energy range from 0.5 to 10 MeV. Furthermore, the capability of using the characteristic X-rays following high energy electron impact ionization for elemental analysis has never been explored. The intent of this research was to provide the experimental measurements necessary 1) to make a critical evaluation of the only existing theoretical calculation, 2) to accumulate a sufficient amount of data to justify future theoretical calculations and with which they may be compared, and 3) to establish that high energy electron impact ionization can be developed into a useful method for quantitative elemental analysis. Hopefully, these efforts will also stir the current experimental and theoretical lethargy to the subject.

1.1 Electron Impact Ionization

1.1.1 General

Atomic ionization by electron impact has been treated *in extenso* by Mott and Massey (MM65) and Massey and Burhop (MB69). These comprehensive works describe and review the general methods for experimental measurement and theoretical calculation of ionization cross sections, and have provided a critical evaluation, comparison and interpretation of the significant results up to 1967.

Ionizing impacts are those inelastic collisions* which result in the ejection of one or more of any of the atomic electrons. The total cross section for ionization consists of the sum of the contributions from all of the atomic shells. The inner shell contributions can be studied by measurements of the characteristic X-radiation following the electron ejection. The theory of X-ray spectra accounting for the transitions and the approximate intensities of the various X-ray lines is well known [cf. Compton and Allison (CA35), White (W34), Condon and Shortley (CS35), Lindh (L30), and Sandström (S57)]. Once an inner shell vacancy is created it can be filled by either a radiative transition from a higher shell or by a nonradiative rearrangement (Auger effect). For illustrative purposes, consider a vacancy created in a K-shell which can be filled by shifting the vacancy to a higher shell, e.g. the L₂ subshell. The binding energy difference (K-L₂) of the two levels can be released as a K α_2 X-ray or can be transferred to another bound electron,

*Inelastic collisions can also result in excitation which refers to the population of excited atomic states without electron ejection (non-ionizing).

e.g. an L_3 subshell electron which is ejected (Auger electron). The latter process is nonradiative and is referred to as a $K-L_2L_3$ Auger transition. The probability that a vacancy in a given subshell i is filled by a radiative transition is the fluorescence yield, ω_i . The Auger yield, a_i , of the same i -shell is defined as the probability that an electron is emitted when the vacancy is filled from a higher shell. These definitions are directly applicable without complication to the K-shell which contains only two electrons. For vacancies in higher shells, which contain eight or more electrons in several subshells, extreme caution in applying these definitions is necessary. Although the definitions can in principle be applied to each of the subshells, the fluorescence yield for a given subshell is difficult to determine. This results from the fact that usually all of the subshells are ionized simultaneously in some specific ratio and that one usually measures an average for the entire shell. An additional complication is that the original distribution of primary vacancies can change by shifting a vacancy from one subshell to another within a given shell. These non-radiative Auger transitions which occur within a shell are known as Coster-Kronig transitions. For example, the $L_1-L_3M_4$ Coster-Kronig transition indicates that a primary vacancy in the L_1 subshell was transferred to the L_3 subshell with the binding energy difference (L_1-L_3) being carried off by a M_4 electron. The Coster-Kronig transition probabilities, e.g. f_{13} for the $L_1-L_3M_4$ case, depend entirely on whether the transitions are energetically possible. The Coster-Kronig transitions are excluded from the definition for Auger yields since the Auger yield includes only those vacancies transferred to higher shells. The Coster-Kronig yield

(f) is defined as the probability that a vacancy is filled with an electron making a nonradiative transition from a higher subshell in the same shell. From the definitions for fluorescence yield (ω), Auger yield (a) and Coster-Kronig yield (f), it is apparent that for the K-shell:

$$\omega_K + a_K = 1 ;$$

whereas, for the L-shell the following relations must hold:

$$\omega_3 + a_3 = 1$$

$$\omega_2 + a_2 + f_{23} = 1$$

$$\omega_1 + a_1 + f_{12} + f_{13} = 1$$

with

$$\bar{\omega}_L + \bar{a}_L = 1$$

where $\bar{\omega}_L$ and \bar{a}_L are respectively the average fluorescence yield and average Auger yield for the L-shell. As indicated, these Coster-Kronig transitions which change the original distribution of primary vacancies must be considered in obtaining subshell yields from measured average fluorescence yields. Comprehensive reviews of atomic fluorescence yields (including Auger and Coster-Kronig transitions) has been made by Fink, et. al. (FJM66), and more recently by Bambynek, et. al. (BCF72).

Radiative transitions can occur by filling the inner shell vacancy from many of the higher shells. Each given transition has its own characteristic X-ray line. A listing and the Siegbahn notations for the radiative transitions involved in filling a K-shell vacancy follows:

$$K\alpha = K\alpha_1 + K\alpha_2$$

$$K\beta = K\beta'_1 + K\beta'_2$$

$$K\beta'_1 = K\beta_1 + K\beta_3 + K\beta_5$$

$$K\beta'_2 = K\beta_2 + K\beta_4 + \text{transitions from higher levels}$$

$$K\alpha_1 = K-L_3$$

$$K\alpha_2 = K-L_2$$

$$K\beta_1 = K-M_3$$

$$K\beta_2 = K-N_3$$

$$K\beta_3 = K-M_2$$

$$K\beta_4 = K-N_2$$

$$K\beta_5 = (K-M_4) + (K-M_5)$$

The radiative transition probabilities are simply proportional to the number of emitted X-rays for the transition. These transition probabilities are measured and reported as ratios. For example, the transition probability ratio for $K\beta/K\alpha$ is just the number of $K\beta$ X-rays to the number of $K\alpha$ X-rays emitted in filling the K-shell vacancies.

With a knowledge of the fluorescence yields and the radiative transition probabilities, the cross sections for a given inner shell ionization can be determined from a measurement of the intensity of only one of the X-rays following the filling of the vacancy. For example, the number of $K\alpha$ X-rays produced by impact of N_e electrons with energy E on a target containing N_a atoms per square centimeter of element Z is

$$N_{K\alpha} = N_e(E) N_a(Z) \frac{\sigma_K(Z, E) \omega_K(Z)}{[1 + \frac{K\beta}{K\alpha}(Z)]}, \quad (1.1)$$

where $\omega_K(Z)$ is the K-shell fluorescence yield for element Z , $K\beta/K\alpha(Z)$ is the transition probability ratio of $K\beta$ to $K\alpha$ X-rays for element Z , and $\sigma_K(Z, E)$ is the K-shell ionization cross section for element Z at

energy E . This theoretical value for $N_{K\alpha}$ is not necessarily the true number of $K\alpha$ X-rays produced. A number of factors are involved which can alter the theoretical production. These are:

1. The production can be enhanced by the unaccounted collisions due to the additional N_e which results from the diffusion and back-diffusion of electrons in the target.
2. The X-rays can be produced with a varying cross section if the electrons are not monoenergetic. Electron energy losses can result from interactions in the target.
3. The production can also be enhanced by fluorescence from bremsstrahlung produced in the target or by fluorescent radiation from higher Z elements in the target or target backing.

Similarly, the measured number of X-rays is not necessarily equal to the true number produced. To obtain the true production from the measured value, correction for the following factors is necessary:

4. The absorption of the X-rays in the target itself.
5. The overall detection efficiency for the X-rays leaving the target, which includes the effects of solid angle, attenuation by materials interposed between the target and the detector, and the intrinsic efficiency for the detector.

By using thin targets ($0.1\text{-}1.0 \text{ mg/cm}^2$) at electron energies of several MeV, the production corrections (1, 2, and 3) can be reduced to a few percent or less. At these high electron energies, the path length for the electron in traversing the target is not much greater than the

target thickness and the fractional electron energy loss is small. This makes the corrections for factors (1) and (2) rather negligible. The bremsstrahlung correction (3) becomes increasingly important at high energies and with high atomic number targets. The correction for the absorption in the target (4) is determined entirely by the composition of the target. The size of this can be estimated for a given target by supplemental transmission measurements. The correction for the overall detection efficiency (5) is fixed for a given geometry and detector. A more thorough description of these corrections is provided in the Results and Discussion (Part 3).

Thus, the cross sections for inner shell ionization by electron impact can be determined from a measurement of the intensity of one of the characteristic X-rays after the appropriate corrections are made. Obviously, relative measurements of these cross sections for a given element as a function of electron energy are much simpler than absolute determinations since many of the corrections would not be necessary. This is also the case, but to a smaller extent, for relative cross section measurements of various elements at a fixed electron energy. The absolute measurements require the inherently difficult task of determining the absolute number of electrons incident on the target. Furthermore, these cross section determinations must be preceded by a knowledge of accurate values for the fluorescence yields and transition probabilities. It is for this reason that most cross section studies have been restricted to the K-shell. The complications in obtaining reliable data for higher shells was discussed above [see also Fink, et. al. (FJM66)]. The following Sections contain a review of prior theoretical

and experimental studies of K-shell ionization cross sections, and the K-shell fluorescence yields and radiative transition probabilities necessary for an experimental determination of the ionization cross sections.

1.1.2 K-Shell Ionization Cross Sections

Theoretical non-relativistic calculations of cross sections for K-shell ionization by fast electron impact have been extensive. Early calculations, made mainly in the 1930-1940 decade, used the Born approximation and non-relativistic electron wavefunctions. These studies are represented by the work of Bethe (B30), Massey and Mohr (MM33), Soden (S34), Massey and Burhop (MB35), Wetzel (W33) and Burhop (B40). The first relativistic calculations were made by Arthurs and Moiseiwitsch (AM58) and Perlman (P60) using the Møller modification of the Born approximation. Arthurs and Moiseiwitsch employed relativistic wavefunctions for the incident electron and non-relativistic wavefunctions for the atomic electron; whereas, Perlman used completely relativistic wavefunctions for both electrons. Usually, these calculations are not in a simple analytical form, but require a difficult normalization of the wavefunctions and a numerical evaluation of the interaction matrix elements to determine the cross sections. The general theory and methodology for these calculations have been described by Mott and Massey (MM65) and Massey and Burhop (MB69). The Kolbenstvedt (K67) theory is the most recent relativistic calculation and departs from the general procedure of the earlier work. Kolbenstvedt derived simple approximate formulae for the cross sections using the Weizsäcker-Williams virtual

photon method combined with the photoelectric cross section for large impact parameters and the Møller cross section for small impact parameters. Only the relativistic calculations are considered here for comparison to experimental measurements at relativistic electron energies greater than 0.5 MeV.

Arthurs and Moiseiwitsch (AM58) used Møller's (M32) modification of the Born approximation [cf. (MM65), p. 810] with suitable wavefunctions to calculate a numerical parameter S. They used relativistic free-particle Darwin (D28) wavefunctions [cf. (MM65, p. 219 ff.)] for both the initial and final states of the incident electron, a non-relativistic hydrogenic Darwin wavefunction for the initial state of the atomic electron and a Coulomb wavefunction for its final state. The parameter S was defined by

$$S = \left[\frac{(Z_e)^2 (\gamma - 1)}{\alpha^2 \pi a_0 \gamma^2} \right]^{\sigma_K}, \quad (1.2)$$

where Z_e is the effective nuclear charge for the K-shell, α is the fine structure constant, a_0 is the hydrogen Bohr radius, σ_K is the K-shell ionization cross section, and $\gamma = (1 - v^2/c^2)^{-\frac{1}{2}}$ where v is the initial velocity of the incident electron. Values of S were tabulated as a function of the ratio of electron kinetic energy E to K-shell ionization energy I_K . Cross sections for values of E from 2.5 to 20 times I_K can be obtained from the tabulated S values using

$$\sigma_K = \frac{S(E/I_K)}{q}, \quad (1.3)$$

where $q = \frac{(2.128 \times 10^{-4})(Z - 0.3)^2 [(E + 1)^2 - 1]}{(E + 1)^2}$. (1.4)

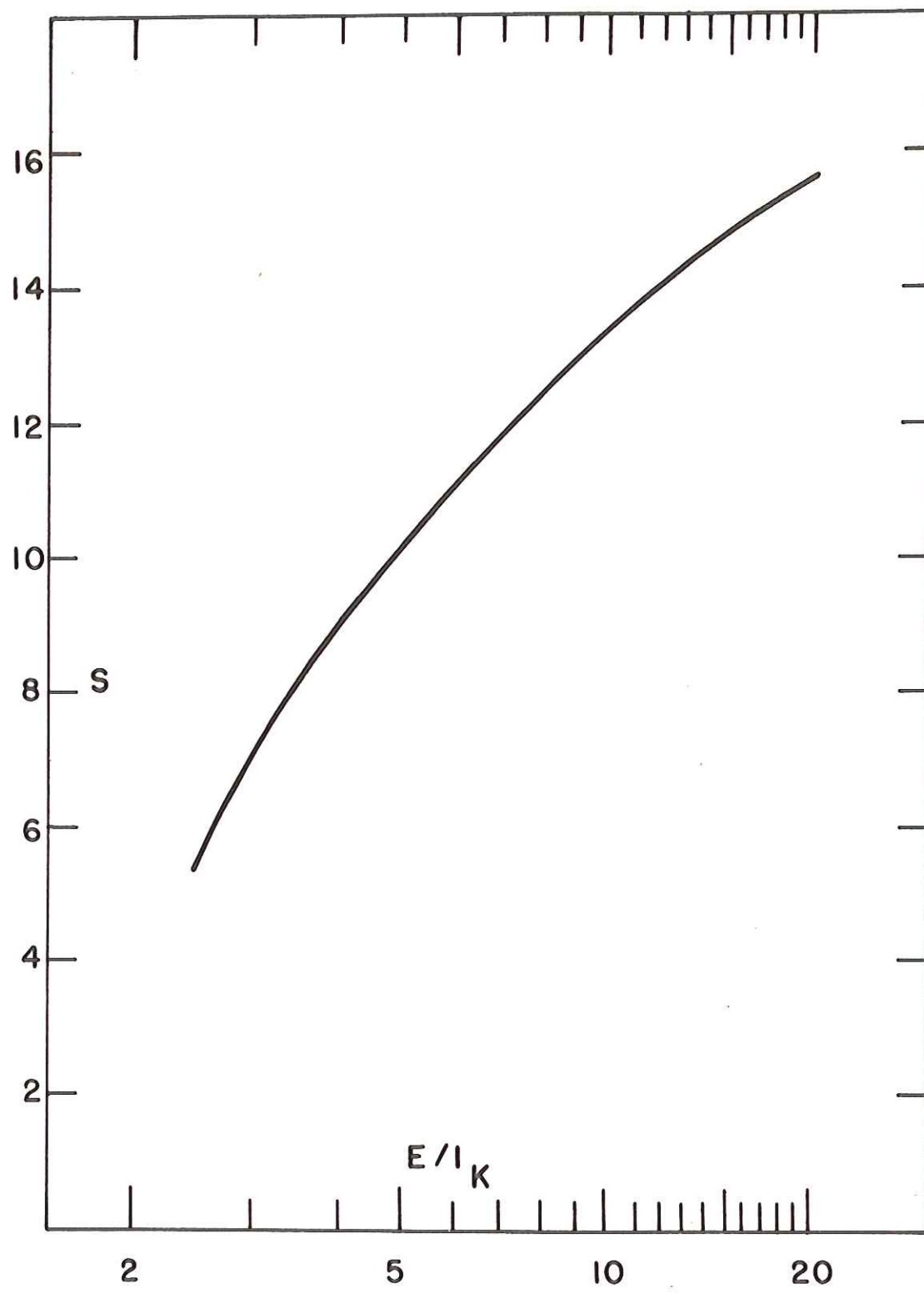
The parameter $S(E/I_K)$ as a function of the E/I_K energy ratio is presented in Figure 1.1. In the above expressions, E is in rest mass units and σ_K is in units of barns. Equation 1.4 was obtained using $a_0 = 0.53 \times 10^{-8}$ cm and assuming Slater-type screening for the effective nuclear charge Z_e of the K-shell, i.e. $Z_e = (Z - 0.3)$. The simple non-relativistic form of the wavefunction used for the initial state of the atomic bound electron restricts the calculation to values of small Z . For large Z , relativistic effects become increasingly important. Furthermore, several assumptions were made in their derivation of Møller's cross section which also places a restriction on the calculation. It was assumed that $(Z_e/\alpha)^2 \ll 1$ and $p \ll 1$ where p is the momentum (in rest mass units) transferred to the atom.

Perlman (P60) calculated the cross sections only for nickel and mercury for incident electron energies from 3 to 18 times the K-shell ionization energy. He also used Møller's relativistic theory with relativistic free-particle Darwin wavefunctions for the incident electron. For the atomic electron, he used more complex relativistic wavefunctions. The initial states were represented by relativistic hydrogenic Darwin and Dirac wavefunctions for nickel and mercury, respectively. A relativistic Coulomb wavefunction was used for the final states of both. Although Perlman discussed the effect of electron exchange [cf (MM65), p. 507 ff.], he did not consider it in the calculations. In comparison to Arthurs and Moiseiwitsch (AM58) and the earlier non-relativistic theories, the completely relativistic calculations of Perlman are expected to give the most accurate values for the cross sections.

FIGURE 1.1

Theoretical Cross Section Parameter (S) as a Function
of the Ratio of the Electron Kinetic Energy (E)
to the K-Shell Ionization Energy (I_K)

The parameter S is taken from the Calculations of Arthurs
and Moiseiwitsch (AM58).



Kolbenstvedt (K67) separated the total K-shell ionization cross section into contributions from "close" and "distant" collisions. Distant collisions were taken as those with an electron impact parameter b greater than the K-shell atomic radius a . Similarly, close collisions were taken as those with b less than a . For the distant collisions ($b > a$), the incident electrons were treated as a spectrum of virtual photons [cf. Jackson (J62), p. 520 ff.] with a field equivalent to that seen by the atomic nucleus for the electron-atom interaction. This field as given by classical electrodynamics is approximately

$$N_k dk \approx \frac{2\alpha}{\pi} \left[\frac{dk}{\beta^2 k} \right] \ln \left(\frac{k_o}{k} \right) , \quad (1.5)$$

where α is the fine structure constant, k is the photon energy, and β is the electron velocity. The parameter k_o is the highest energy taken into consideration and is related by

$$k_o = \frac{1.123\beta}{b_o \sqrt{1 - \beta^2}} \exp(-\frac{1}{2}\beta^2) \quad (1.6)$$

to the smallest impact parameter b_o considered ($b_o = a$). With the electrons treated as virtual photons, ionization of the atom occurs by the photoelectric effect. The contribution to the K-shell ionization energy is therefore given by

$$\sigma_{\text{distant}} = \int_{I_K}^{k_o} \sigma_k N_k dk , \quad (1.7)$$

where the integration limits are from I_K , the K-shell ionization energy, to k_o , the assumed upper energy limit. The photoelectric cross section σ_k used by Kolbenstvedt was a simple non-relativistic approximation [Born approximation, cf. Heitler (H54), p. 208] for two K-shell electrons

in a hydrogenic atom. It is given by,

$$\sigma_k = \frac{128\pi}{\alpha^3 Z^2} \left(\frac{I_K}{k} \right)^4 \frac{\exp(-4\zeta \arccot \zeta)}{1 - \exp(-2\pi\zeta)} \sigma_0 , \quad (1.8)$$

where

$$I_K = \frac{1}{2}(\alpha Z)^2 ,$$

$$\sigma_0 = \left(\frac{8\pi}{3} \right) r_0^2 ,$$

and

$$\zeta = I_K / (k - I_K) .$$

Because Equation 1.8 was obtained from a Born approximation plane wave analysis instead of using exact wavefunctions for the virtual photon spectrum, the calculation for $\sigma_{distant}$ is restricted. It is not valid for heavy elements or for low energy virtual photons when the energy of the ejected electron and I_K can be comparable. In solving the integral of Equation 1.7, an approximation was also made as to the important energy interval in the integral. For the close collisions ($b < a$), Kolbenstvedt used the well known Møller cross section formula for the collision between two free electrons (i.e. the atomic electron is assumed to be at rest). This is given by,

$$d\sigma_M = \frac{2\pi r_0^2}{\beta^2(\epsilon-1)} \left\{ \frac{1}{W^2} + \frac{1}{(1-W)^2} + \left(\epsilon - \frac{1}{\epsilon} \right)^2 - \left(2\epsilon - \frac{1}{\epsilon^2} \right) \frac{1}{W(1-W)} \right\} dW , \quad (1.9)$$

where $\epsilon = 1/1-\beta^2$, and W is the ratio between the transferred energy and the kinetic energy of the incident electron. The close collision contribution is therefore given by,

$$\sigma_{close} = 2 \int_{W=I/(\epsilon-1)}^{W=\frac{1}{2}} d\sigma_M . \quad (1.10)$$

Approximations made in the solution of the integral as well as the interpretation for the choice of the integration limits were described by

Kolbenstvedt. The total K-shell ionization cross section is taken as the sum of σ_{distant} and σ_{close} . Simple analytical formulae derived by Kolbenstvedt for the two contributions are

$$\sigma_{\text{distant}} = \frac{0.275}{I_K} \frac{(E+1)^2}{E(E+2)} \left[\ln \left(\frac{1.19 E(E+2)}{I_K} - \frac{E(E+2)}{(E+1)^2} \right) \right] \quad (1.11)$$

and

$$\begin{aligned} \sigma_{\text{close}} = & \frac{0.99}{I_K} \frac{(E+1)^2}{E(E+2)} \left[1 - \frac{I_K}{E} \left(1 - \frac{E^2}{2(E+1)^2} \right. \right. \\ & \left. \left. + \frac{2E+1}{(E+1)^2} \ln \frac{E}{I_K} \right) \right], \end{aligned} \quad (1.12)$$

where I_K and $E = (\epsilon - 1)$ are expressed in rest mass units, and the cross sections are in barns. Although the formulae (Equations 1.11 and 1.12) were derived assuming $I_K = \frac{1}{2}(\alpha Z)^2$, Kolbenstvedt used experimental values of I_K in his calculations and in comparing them with experiments. This was done to "very crudely" take into account the effect of outer shell electron screening. Recently, Kolbenstvedt revised his calculations for comparison with cross section measurements made at extremely relativistic electron energies ($E = 150 - 900$ MeV). The revision and these measurements have been described by Middleman, Ford and Hofstadter (MFH70).

Cross section measurements for K-shell ionization by electrons in the energy range from 0.5 MeV to 10 MeV have been rather sparse. Considerably more effort has been made in the energy range below 0.5 MeV [cf. Massey and Burhop (MB69), p. 165]. Most of these experimental studies however, have been limited to electron energies of less than several hundred keV, and to atomic numbers less than 50. Below 10 keV, the number of investigations has been extensive [cf. Kieffer (K69) and

Kieffer and Dunn (KD66)]. The only measurements for electrons above 10 MeV, have been the ultra-high energy (150-900 MeV) studies of Middleman, Ford and Hofstadter (MFH70).

Table 1.1 contains all of the known measurements of K-shell ionization cross sections σ_K with electrons between 0.5 and 10 MeV. As indicated, only the elements zirconium ($Z = 40$), palladium ($Z = 46$), silver ($Z = 47$), tin ($Z = 50$), tungsten ($Z = 74$), gold ($Z = 79$), and lead ($Z = 82$) have been studied. The experimental values are compared to the theoretical calculation of Kolbenstvedt (K67) and where applicable to the theories of Arthurs and Moiseiwitsch (AM58) and Perlman (P60). Motz and Placous (MP64) measured σ_K for tin and gold at 0.5 MeV and at several lower electron energies. Hansen, Weigmann and Flammersfeld (HWF64) measured σ_K for zirconium, tin, tungsten and lead at five electron energies from 0.24 MeV to 1.44 MeV. Rester and Dance (RD66) measured σ_K for tin and gold up to 2.0 MeV, and for silver up to 1.0 MeV. Recently, Berkner, Kaplan and Pyle (BKP70) reported measurements of σ_K for palladium and gold at energies of 2.5 and 7.1 MeV. The trends of the experimental values of σ_K as a function of electron energy and atomic number suggests reasonable agreement among all of the measurements except those of Hansen, et. al. (HWF64). When direct comparison is possible, their values are much larger than those of the others by amounts exceeding five times the estimated uncertainties (10-15%). In the regions where Arthurs and Moiseiwitsch (AM58) calculations are applicable ($3 \leq E/I_K \leq 20$), their results and those of Kolbenstvedt (K67) are in good agreement. The calculations of Perlman (P60) for mercury can be compared to the experimental results of Motz and Placous (MP64) and

Table 1.1

Comparison of Experimental and Theoretical K-Shell Ionization Cross Sections (σ_K) for Relativistic Electrons with Energy (E), $0.5 \text{ MeV} \leq E < 10 \text{ MeV}$

	E (MeV)	Experimental σ_K^* (barns)			Theoretical σ_K (barns)			
					(AM58)	(P60) ⁺	(K67)	
Zr (Z = 40)	0.53	115	\pm	8	(HWF64)	-	-	73.0
	0.82	125	\pm	9	(HWF64)	-	-	71.2
	1.13	115	\pm	9	(HWF64)	-	-	71.6
	1.44	99	\pm	10	(HWF64)	-	-	72.7
Pd (Z = 46)	2.50	71	\pm	7	(BKP70)	-	-	55.2
	7.10	78	\pm	8	(BKP70)	-	-	65.0
Ag (Z = 47)	1.00	47	\pm	5	(RD66)	-	-	47.7
Sn (Z = 50)	0.50	41	\pm	5	(MP64)	38.9	-	40.9
	0.53	61	\pm	3	(HWF64)	38.6	-	40.8
	0.60	40	\pm	4	(RD66)	37.6	-	40.5
	0.80	39	\pm	4	(RD66)	-	-	40.5
	0.82	68	\pm	4	(HWF64)	-	-	40.5
	1.00	39	\pm	4	(RD66)	-	-	40.8
	1.13	72	\pm	4	(HWF64)	-	-	41.1
	1.20	40	\pm	4	(RD66)	-	-	41.3
	1.40	42	\pm	4	(RD66)	-	-	41.9
	1.44	72	\pm	4	(HWF64)	-	-	42.0
	1.70	43	\pm	4	(RD66)	-	-	42.8
	2.00	44	\pm	4	(RD66)	-	-	43.7
W (Z = 74)	0.53	23.8	\pm	2.5	(HWF64)	13.8	-	13.4
	0.82	34.5	\pm	3.5	(HWF64)	14.1	-	14.1
	1.13	34.0	\pm	3.5	(HWF64)	14.5	-	14.8
	1.44	24.9	\pm	3.8	(HWF64)	14.5	-	15.4
Au (Z = 79)	0.50	12.5	\pm	2	(MP64)	11.4	7.8	10.8
	0.60	10	\pm	1	(RD66)	11.5	8.0	11.1
	0.80	10	\pm	1	(RD66)	11.8	8.5	11.7
	1.00	10	\pm	1	(RD66)	12.1	9.0	12.1
	1.20	10	\pm	1	(RD66)	12.3	9.3	12.5
	1.40	10	\pm	1	(RD66)	12.5	11.0	12.8
	1.70	11	\pm	1	(RD66)	-	-	13.3
	2.00	11	\pm	1	(RD66)	-	-	13.7
	2.50	11	\pm	1	(BKP70)	-	-	14.3
	7.10	14	\pm	1	(BKP70)	-	-	17.5

Table 1.1 (Continued)

E (MeV)	Experimental σ_K^* (barns)	Theoretical σ_K (barns)		
		(AM58)	(P60) ⁺	(K67)
Pb (Z = 82)				
0.53	18.7 ± 2.8 (HWF64)	10.2	-	9.7
0.82	25.5 ± 3.5 (HWF64)	10.7	-	10.5
1.13	26.0 ± 3.5 (HWF64)	11.2	-	11.1
1.44	24.8 ± 5.0 (HWF64)	11.5	-	11.6

*In parentheses are the references from which the values were taken.

⁺Calculated for Z = 80.

Rester and Dance (RD66) for the case of gold ($Z = 79$) and to theories of Arthurs and Moiseiwitsch (AM58) and Kolbenstvedt (K67). Although the prediction of Perlman (P60) is in excellent agreement with the experimental values at ~ 1.0 MeV, the energy dependence at both lower and higher energies is in marked disagreement with both the experimental measurements and the other theoretical calculations. This is surprising since the completely relativistic calculations of Perlman (P60) should be expected to give more accurate σ_K values than the semi-relativistic calculations of Arthurs and Moiseiwitsch (AM58) or the simplified theory of Kolbenstvedt (K67). Motz and Placious (MP64) have suggested that perhaps there are errors in the numerical evaluation of Perlman's complicated formulae. The theories of Arthurs and Moiseiwitsch (AM58) and Kolbenstvedt (K67) do not agree in absolute magnitude with the experimental values, but the trend of the energy dependence is well represented by both of these calculations. It should also be recognized that for low electron energies and light elements where relativistic effects are unimportant, non-relativistic calculations [e.g. those of Burhop (B40)] are in good agreement with both the calculations of Arthurs and Moiseiwitsch (AM58) and the experimental σ_K values [cf. Massey and Burhop (MB69), p. 166]. Perhaps, it should also be pointed out that the measurements at the ultra-high electron energies of 150-900 MeV are in excellent agreement with a revised Kolbenstvedt calculation (MFH70). In general, there appears to be little difference in the results between the theories of Arthurs and Moiseiwitsch (AM58) and Kolbenstvedt (K67) when the former is applicable, but the Kolbenstvedt theory has the singular advantage of being the only calculation valid for the entire

periodic range of elements and all incident electron energies.

Typical theoretical K-shell ionization cross sections calculated by the Kolbenstvedt theory (K67) are provided in Figures 1.2 and 1.3. These results were obtained using experimental critical absorption X-ray energies (FH55) for the K-shell ionization energies in the formulae of Equation 1.11 and 1.12. Figure 1.2 contains the theoretical σ_K values as a function of electron energy from 0.1 MeV to 10 MeV for aluminum ($Z = 13$), nickel ($Z = 28$), tin ($Z = 50$) and gold ($Z = 79$). As shown, the cross sections are very smooth and slowly varying functions of the electron energy over the entire range. The cross section dependence as a function of atomic number for 2 MeV electrons is shown in Figure 1.3. Although the cross sections have a smooth functional dependence over the entire range of elements, they decrease rapidly from about 2000 barns at $Z = 10$ to approximately 12 barns at $Z = 83$.

1.1.3 K-Shell Fluorescence Yields

Until very recently (circa 1972), the "best" values for K-shell fluorescence yields were obtained from the well known "best fit" theoretical curve in the comprehensive review by Fink, Jopson, Mark and Swift (FJM66). This theoretical curve was obtained from the calculations of Callen (C63) and Listengarten (L62) and was considered to be more reliable than many of the experimental measurements made up to that time. Those experimental values which were considered to have been more accurately measured appeared to agree best with the theoretical curve. Fink [see reference (13) in McGuire (M70)] has reported that most of the experimental values compiled in their 1966 review (FJM66) cannot

FIGURE 1.2

Theoretical K-Shell Ionization Cross Section (σ_K)
as a Function of Electron Energy for
Aluminum, Nickel, Tin and Gold

Calculated by Kolbenstvedt (K67) theory using experimental
critical absorption X-ray energies (FH55) for the K-shell
ionization energies.

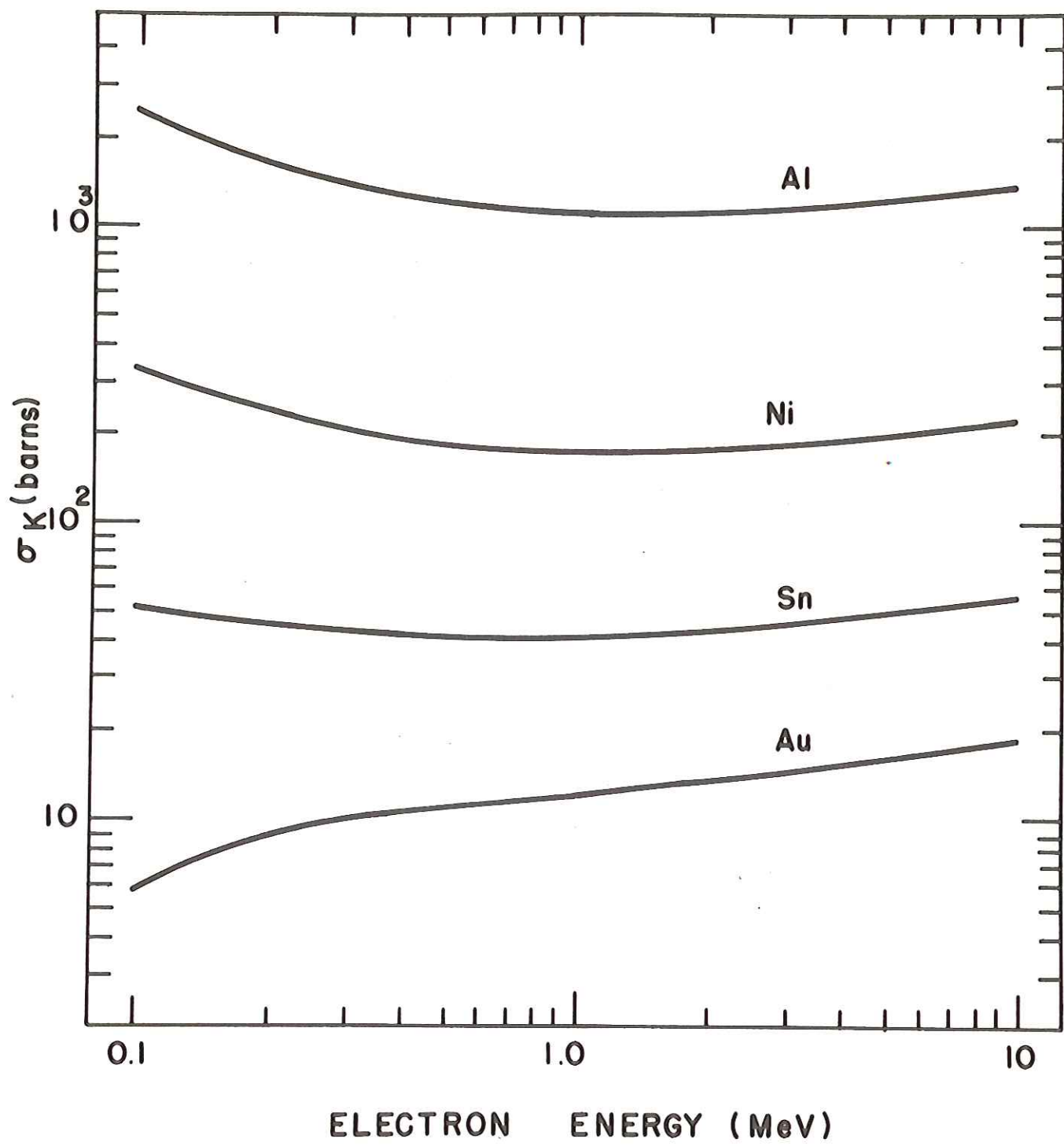
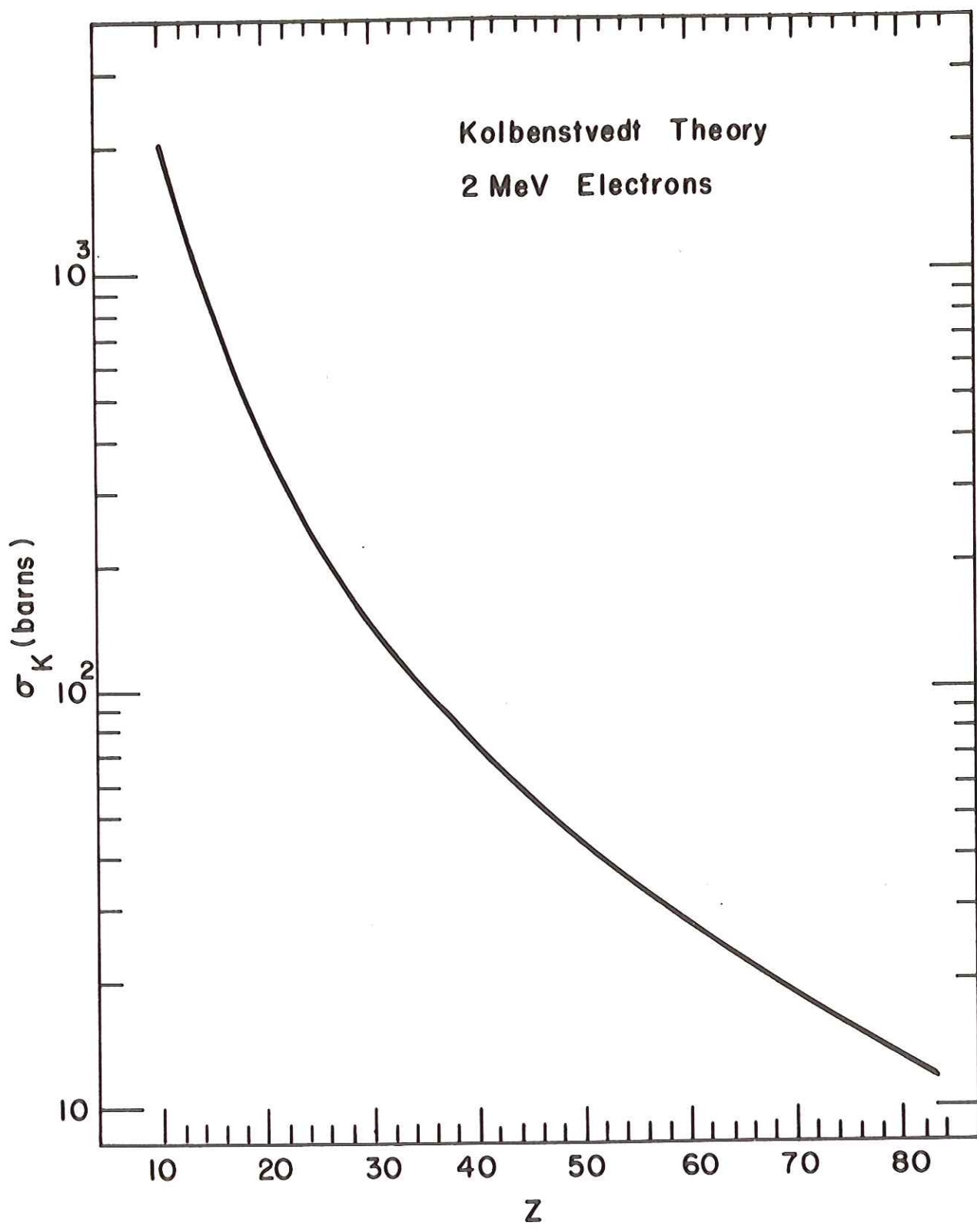


FIGURE 1.3

Theoretical K-Shell Ionization Cross Sections (σ_K)
as a Function of Atomic Number (Z)
for 2 MeV Electrons

Calculated by Kolbenstvedt (K67) theory using experimental
critical absorption X-ray energies (FH55) for the K-shell
ionization energies.



withstand critical experimental scrutiny. Since then however, numerous precision measurements have been made. Bambynek, Crasemann, Fink, et. al. (BCF72) have recently "critically evaluated" these measurements and the "most reliable" were fitted to Burhop's (B55) semi-empirical fitting function:

$$\omega_K = \frac{[a + bZ + cZ^3]^4}{1 + [a + bZ + cZ^3]^4} \quad (1.13)$$

to derive a complete set of what are "probably the best ω_K values known to man".[†] These fitted values (BCF72) have made it possible to make critical comparisons with theoretical calculations. Three of the most recent and accurate calculations are those of McGuire (M70), Walters and Bhalla (WB71), and Kostroun, Chen and Crasemann (KCC71). A comparison of their results and those of several earlier (B35, RS55, C63) calculations is provided in Figure 1.4. As shown, the general features of the results for all the modern calculations are in good agreement. In the medium Z region from $Z = 35$ to $Z = 50$, there are virtually no differences in the calculations. In general, the calculations of Kostroun, et. al. (KCC71) agree best with "reliable" experimental values. A comparison of their results with the "most reliable" critically evaluated experimental ω_K values compiled by Bambynek, et. al. (BCF72) is shown in Figure 1.5. The semi-empirical set of ω_K values derived from a best fit of Equation 1.13 to the "most reliable" experimental values is also shown. In the range from $Z = 10$ to $Z = 50$, the result of Kostroun, et. al. (KCC71) are in very good agreement with the experimental and

[†]B. Crasemann, private communication, 1972.

FIGURE 1.4

Theoretical K-Shell Fluorescence Yields (ω_K)
as a Function of Atomic Number (Z)

The calculations are those of Burhop (B35), Rubenstein and Snyder (RS55), Callen (C63), McGuire (M70), Kostroun, Chen and Crasemann (KCC71), and Walters and Bhalla (WB71). This figure is taken in whole from Reference BCF72.

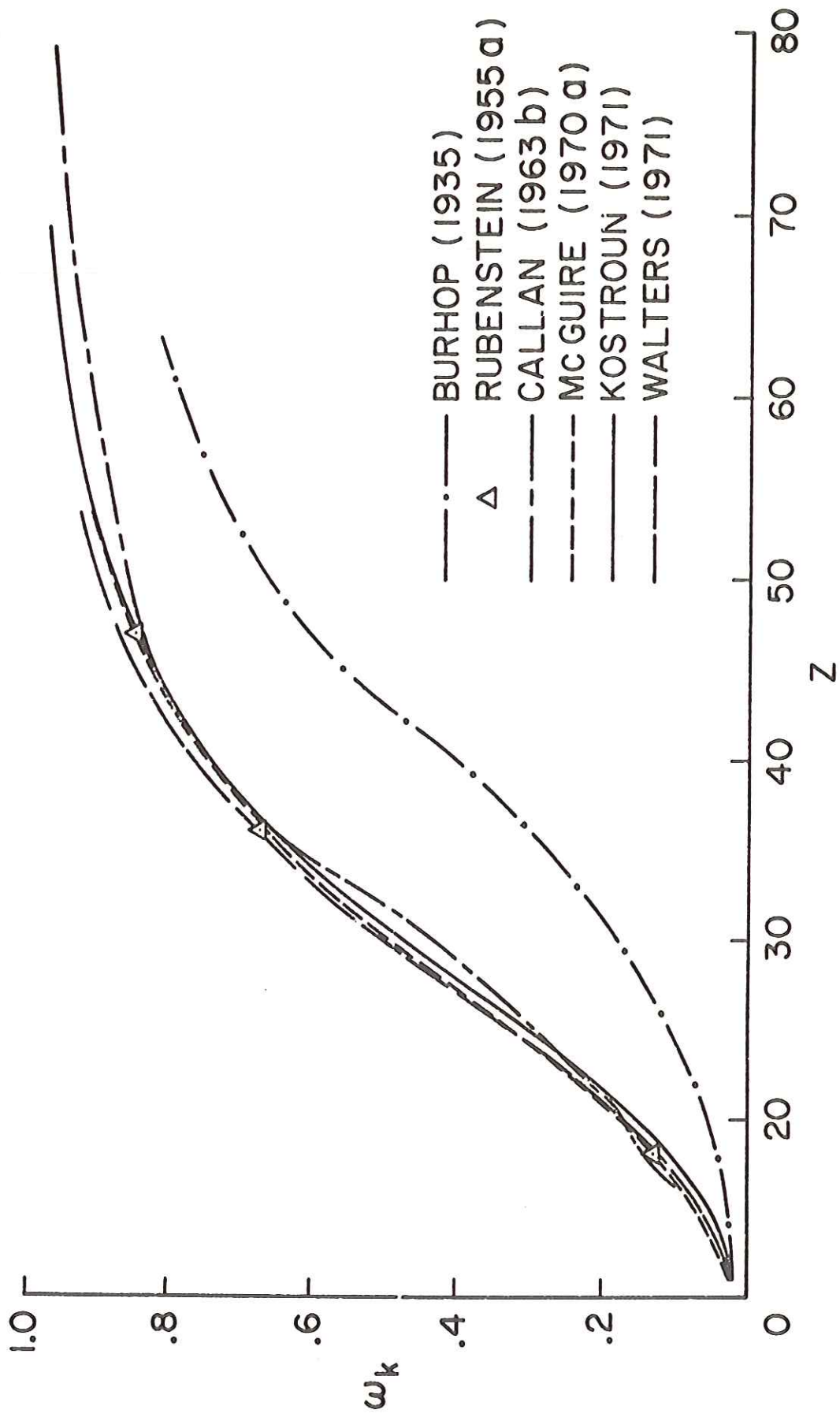
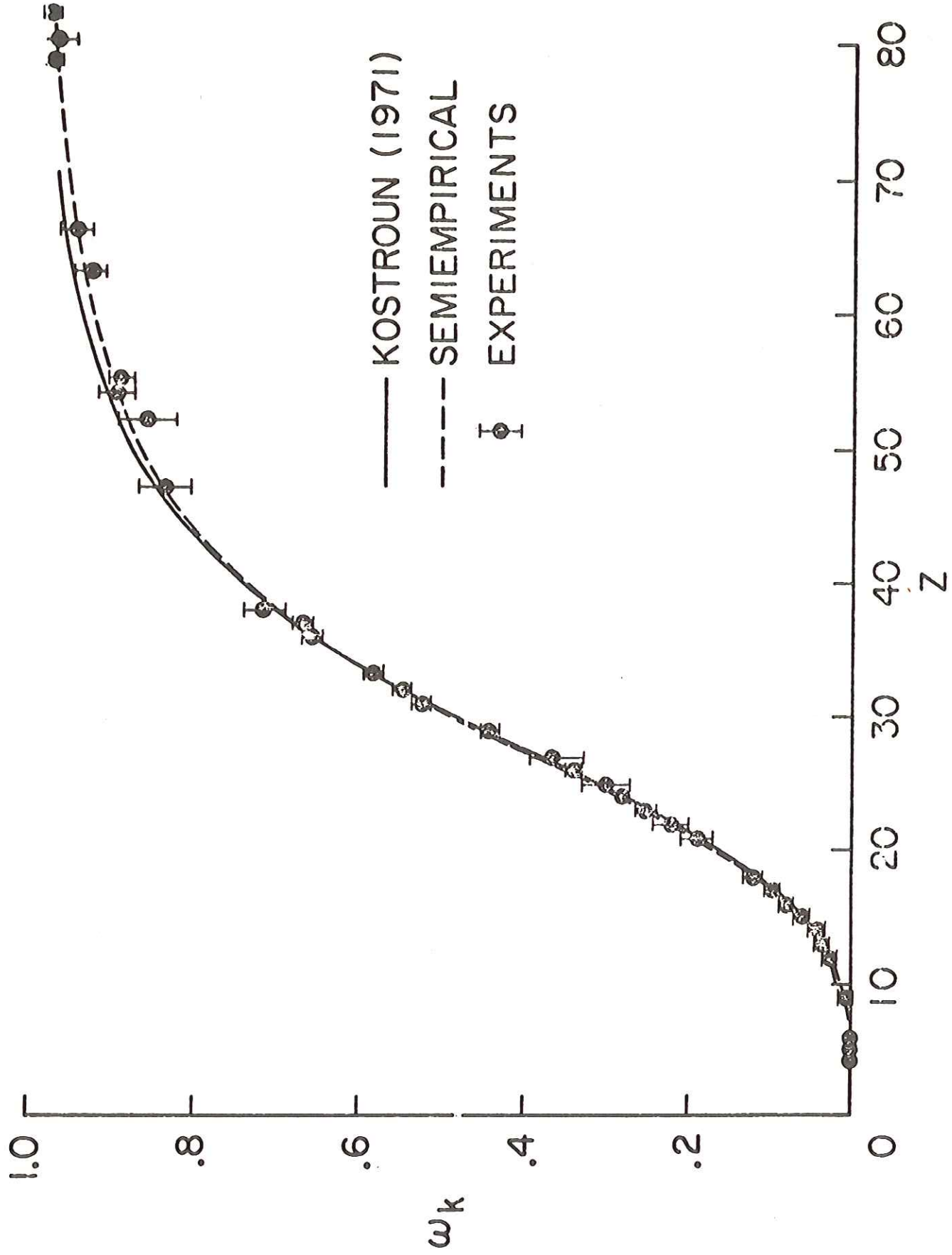


FIGURE 1.5

Theoretical and Experimental K-Shell Fluorescence
Yields (ω_K) as a Function of Atomic Number (Z)

The theoretical values are those from the calculations of Kostroun, Chen and Crasemann (KCC71). The data points are "most reliable" critically evaluated experimental results compiled by Bambynek, Crasemann, Fink, et. al. (BCF72). The dashed curve represents the set of ω_K values derived from a best fit of Equation 1.13 to the selected experimental results. This figure is taken in whole from Reference BCF72.



semi-empirical values. Above $Z = 50$, they tend to be slightly higher, because relativistic effects were neglected in the calculations. It is anticipated that the small remaining systematic discrepancies will be resolved in the near future (BCF72).

A complete review of all the prior experimental and theoretical work on fluorescence yields has recently been provided by Bambynek, et. al. (BCF72). As mentioned above, they have constructed a complete set of reliable ω_K values over the entire periodic range of elements. This set will undoubtedly become the "standard" for at least the next several years until even more precision measurements become available.

1.1.4 K-Shell Radiative Transition Probability Ratios

Nelson, Saunders and Salem (NSS70) have recently tabulated "best" values of transition probability ratios for X-rays following a K-shell vacancy. They obtained these values by drawing smooth curves through recent experimental measurements when the data was plotted as functions of atomic number. They tabulated values for the ratios $K\alpha_2/K\alpha_1$, $K\beta_3/K\beta_1$, $(K\beta_1 + K\beta_3)/K\alpha_1$, $K\beta'_1/K\alpha_1$, $K\beta'_2/K\alpha_1$, and $K\beta/K\alpha$ and compared them with the values adopted by Wapstra, Nijgh and van Lieshout (WNL59) in 1959 and with the recent theoretical calculations of Scofield (S69). For the $K\beta/K\alpha$ ratios*, the measurements of Slivinsky and Ebert (SE69) and Hansen, Freund and Fink (HFF70) were used to obtain the "best" values. In general, both sets of experimental measurements agree within their stated error limits (3-5%). In comparison, the theoretical values

*These are the only values of interest for this study.

of Scofield (S69), which are in good agreement with the Wapstra, et. al. (WNL59) curves between $Z = 30$ and $Z = 70$, are low by as much as 10-15% from the recent measurements. A plot of the $K\beta/K\alpha$ ratio as a function of atomic number showing the experimental measurements, Scofield calculation, and "best" value curve of Nelson, et. al. is provided in Figure 1.6. The smooth curve fitted by Nelson, et. al. deviates from any given measurement by only several percent. Therefore, their tabulated values are expected to be reasonably reliable for all elements from $Z = 20$ to $Z = 90$.

1.2 Application to Elemental Analysis

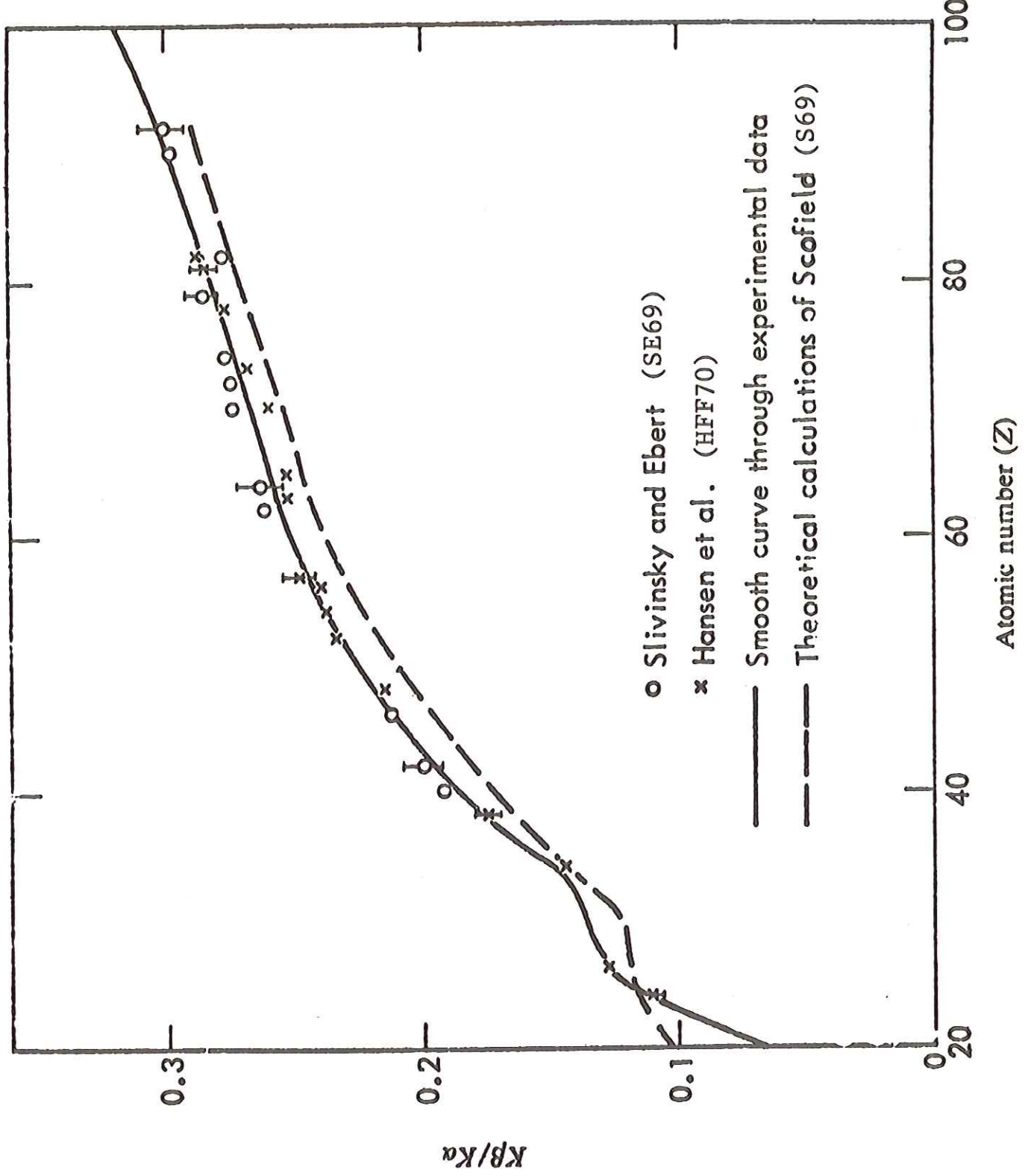
The characteristic X-radiation following high energy electron impact ionization can be used for elemental analysis. The virtues of analysis by X-ray spectrometry need not be cited here since this subject has had extensive treatment. This is reflected by the decades of books, hundreds of comprehensive reviews, and thousands of research papers describing the methods and applications*. The subject is treated in virtually every text, treatise or compendium on instrumental or physical methods of chemical analysis. In fact, it has become so voluminous and

*The reader is referred to the following books which provide a general treatment and survey of the entire field: E. P. Bertin, "Principles and Practise of X-ray Spectrometric Analysis", Plenum, N. Y., 1969; L. S. Birks, "X-ray Spectrochemical Analysis", Second Edition, Interscience, N. Y., 1969; L. S. Birks, "Electron Microprobe Analysis", Interscience, N. Y., 1963; A. H. Compton and S. K. Allison, "X-Rays in Theory and Experiment", Second Edition, Van Nostrand, N. Y., 1935; K. F. J. Heinrich, "The Electron Probe", Wiley, N. Y., 1963; R. Jenkins and J. L. deVries, "Practical X-Ray Spectrometry", MacMillan, London, 1967; R. Jenkins and J. L. deVries, "Worked Examples in X-Ray Spectrometry", MacMillan, London, 1970; R. O. Müller, "Spectrochemical Analysis by X-Ray Fluorescence", Plenum, N. Y., 1972.

FIGURE 1.6

Theoretical and Experimental Transition Probability
Ratios ($K\beta/K\alpha$) as a Function of Atomic Number (Z)

The experimental values are those of Slivinsky and Ebert (SE69), and Hansen, Freund and Fink (HFF70). The solid line is a smooth curve through the experimental data. The theoretical calculation of Scofield (S69) is shown with a broken line. This figure is taken in whole from the compilation of Nelson, Saunders and Salem (NSS70).



specialized that it is now subdivided into many fields depending on the methods of excitation (e.g., by X-ray tubes, radioactive sources, electron microprobe, etc.), the methods of X-ray detection (e.g., by energy dispersive methods or with diffraction analyzing crystals), or the types of applications (e.g., surface analyses, biological and medical analyses, metallurgical and mineralogical analyses, etc.).

In comparison to other excitation methods used for elemental analysis by X-ray spectrometry, high energy electron impact ionization has some distinct advantages. These advantages are characterized by the large range of MeV electrons in solids with a consequent small energy loss in thin samples, and by the smooth variation of the K-shell ionization cross sections with both atomic number and electron energy (see Figure 1.2 and 1.3). The X-ray production from photon excitation methods (X-ray tubes and radioactive sources) can vary rapidly from element to element because of the atomic shell structure effects. For this reason, several X-ray target tubes or several radioactive sources are usually required to cover the entire periodic range of elements (B69, p. 21). In contradistinction to using photon sources, the production yield of X-rays by several MeV electron impact ionization is comparable over the entire range of elements. Consider, for example, the $K\alpha$ X-ray production by 2 MeV electron impact, as reflected by the expression

$$\frac{\sigma_K \omega_K}{(1 + K\beta/K\alpha)},$$

where σ_K is the K-shell ionization cross section taken from Figure 1.3, ω_K is the K-shell fluorescence yield taken from Figure 1.5, and $K\beta/K\alpha$ is the transition probability ratio given in Figure 1.6. This expression

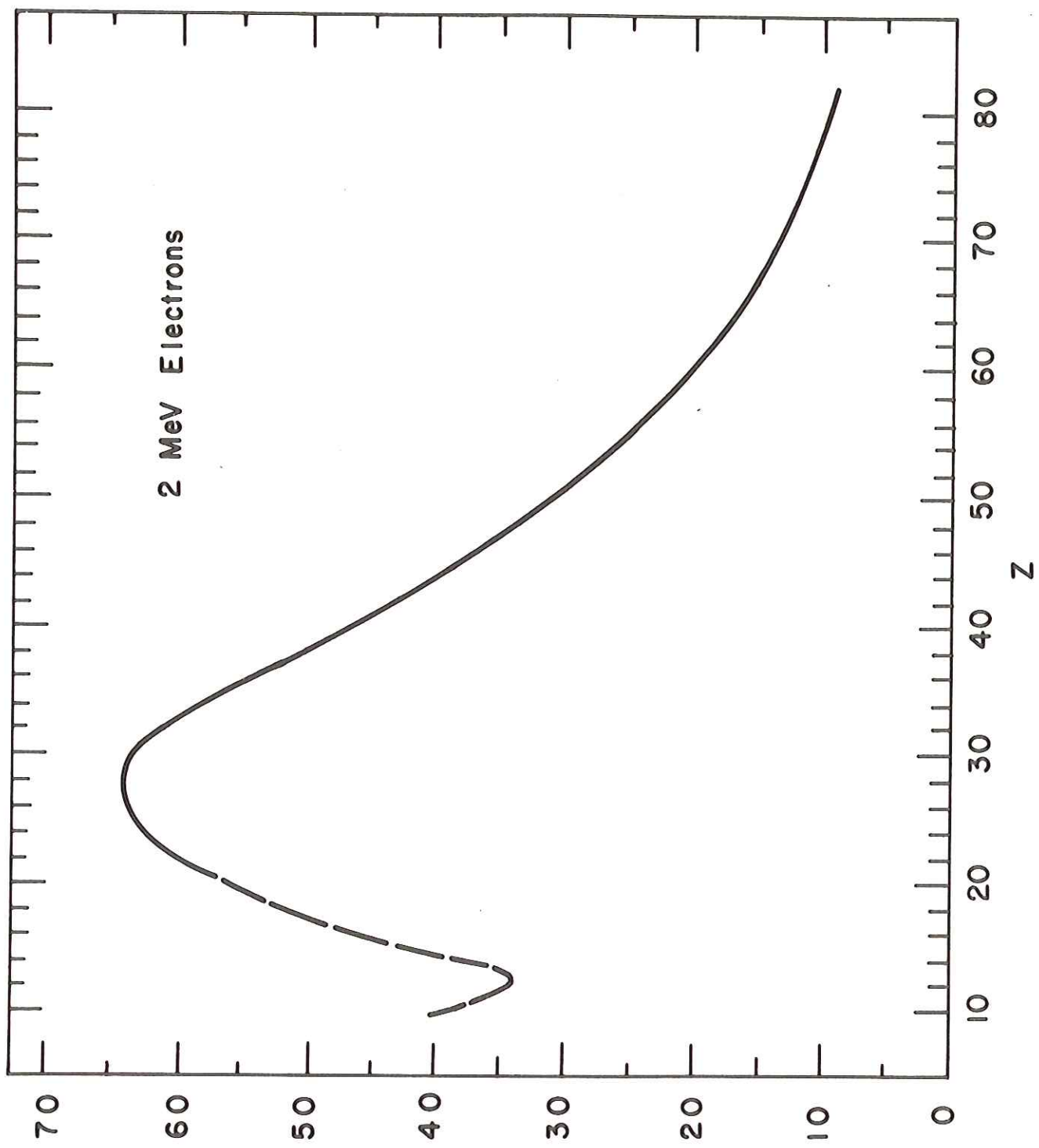
for $K\alpha$ X-ray production as a function of atomic number from $Z = 10$ to $Z = 83$ is given in Figure 1.7. As shown, the production varies smoothly and gradually from ~ 35 barns at phosphorus ($Z = 15$) to a maximum of ~ 65 barns at nickel ($Z = 28$) and decreases to 10 barns at lead ($Z = 82$). An additional feature of the ionization cross sections at several MeV is that even for a change in incident electron energy by several percent, the difference in X-ray production is negligible (see Figure 1.2). Compared to the electron microprobe (B63) or the more recently explored technique of ionization by positive ion impact (JAJ70), high energy electrons enjoy the advantage of a far smaller energy loss per unit length in solid materials. Therefore, the limitations of target preparation are relatively minor, and the general problems of matching unknown and reference sample matrices are less severe. The large range for high energy electrons and their relatively constant (with energy) ionization cross section makes the X-ray production intensity approximately uniform throughout the electron path length in the target. Thus, the entire target thickness is sampled with almost an identical X-ray production efficiency. This is in contrast to the situation for the electron microprobe or positive ion excitation, where iterative approximations are necessary to calculate the X-ray production as a function of the depth of the interaction in the target (B63, p. 112).

For these studies, a simple and rapid method was developed which is based entirely on empirically determined relative X-ray yields. No matrix corrections [cf. Gould and Bates (GB72)] were used in the method to show that excellent approximate quantitative determinations can be obtained without the corrections. This is not possible with

FIGURE 1.7

K α X-Ray Production [$\sigma_K \omega_K / (1 + K\beta/K\alpha)$] as a Function
of Atomic Number (Z) for Ionization
by 2 MeV Electrons

The values for the cross sections (σ_K), fluorescence yields
(ω_K), and transition probability ratios ($K\beta/K\alpha$) were taken
from Figures 1.3, 1.5 and 1.6, respectively.



$$\frac{(1 + K_B/K_a)}{K_w K} \text{ (barns)}$$

excitation by low energy electrons or high energy positive ions where extensive corrections are necessary to obtain even order of magnitude determinations. It must be realized of course, that all of the sophisticated corrections which apply to other X-ray methods can also be implemented in this method.

Quantitative elemental analysis by X-ray spectrometry is effected by relating measured X-ray intensities to the amount of an element in a sample. The simplest approach is to establish the proportionality constant for the relation with pure elements, and then use this constant to determine the amount of that element in an unknown sample. This method, of course, neglects all sample matrix effects which enhance or reduce the X-ray production and which attenuate the X-ray emission intensity. In addition, it requires the normalization of two measurements, i.e., the X-ray intensity for the pure element and that for the unknown. Another possible approach that is frequently used employs comparison standards which closely resemble the unknown. This attempts to account for the deviations from proportionality due to matrix effects, but requires the difficult contrivance of a comparison standard for each unknown or type of unknown. Again, the two measurements for the standard and the unknown must be normalized before comparison can be made.

The procedure adopted for this study incorporates in spirit the major features of both of the above methods, and in addition has one further advantage. Like the first method, it attempts to establish a constant of proportionality between the amount of an element and its X-ray intensity. This is accomplished by determining relative X-ray yields for all the elements with respect to that for a primary reference

element. The relative yields are obtained by simultaneously measuring the X-ray intensities for the primary reference and another element in a reference sample containing a known relative amount of both. In this way, the X-ray yields for all the elements are determined relative to each other. Using these relative yields, relative amounts of the elements in an unknown sample can then be determined from their measured X-ray intensities which are simultaneously obtained from the spectrum of the unknown. Similarly, the fraction of a given element in the total amount of unknown can be determined from the relative yields by adding a known relative amount of an internal reference element to the unknown.

A first order approximation to the comparison standard method is used to eliminate deviations in the yields because of matrix effects. The approach is to get all the unknown and reference samples to resemble each other. This is, of course, impossible in the strictest sense, but in the limit of relatively uniform and thin samples, an adequate approximation should be attainable. The procedure used here to obtain approximately similar targets for the electron irradiation consists of dissolving the solid samples and adsorbing the solutions onto identical thin adsorbent supporting matrices. Due to the unique properties of high energy electrons with respect to range and ionization characteristics, as discussed above, the X-ray production is essentially constant throughout the target thickness. Thus, no corrections for matrix effects are necessary for the primary excitation process. X-ray production from secondary fluorescence and bremsstrahlung generated in the target contributes at most a few percent for targets that are only a few mg/cm^2 thick. Depending on the sample composition, self-absorption

in the target can be an important effect. Still, because of the target preparation method used, the latter two matrix effects are compensated to first order. Furthermore, they can be more easily taken into account because no corrections are necessary for the primary excitation process.*

The additional advantage of this procedure is that it does not require the normalization of two or more measurements. This results from the fact that all of the measurements are relative. For the same reason, once the samples are weighed, the procedure does not require any further absolute measurements, such as for the amount of target material or the number of X-rays. Specific details of the analysis procedure are given in Section 2.4.

Interfering background radiation is not unique to any of the specific excitation methods. Like the electron microprobe, high energy electron impact ionization is limited by the background interference due to electron bremsstrahlung produced in the target. Although bremsstrahlung production is inherently small for positive ions, these projectiles give rise to "knock-on" electrons, which in turn produce low energy bremsstrahlung. Even with the X-ray sources, there is a continuous background due to incoherent Compton scattering of the exciting radiation.

*These matrix effects and corrections are discussed in considerably more detail in the Results and Discussion (Section 3.).

Part 2

EXPERIMENTAL

2.1 SUNY/Albany Dynamitron

The 4 MeV Dynamitron Accelerator at the State University of New York at Albany was used as the source of accelerated electrons. The Dynamitron, manufactured by Radiation Dynamics, consists of an evacuated acceleration tube powered by a constant potential supply. This power supply converts low-voltage ac power to high-voltage dc power by means of a cascaded rectifier system driven in parallel from an RF oscillator. A general description of the Dynamitron and its operation has been provided by Cleland and Morganstern (CM60). The Dynamitron accelerator is mounted horizontally and delivers the accelerated electron beam into a 4 inch diameter stainless steel beam tube. A schematic of the physical arrangement of the Dynamitron beam lines is provided in Figure 2.1. The electron beam is magnetically steered through a permanent 2.54 cm diameter aperture, located at position A in Figure 2.1, and down the zero-degree beam line. Removable apertures located further down-stream could also be used to rigidly define the beam position. The location and use of these removable apertures will be described later.

2.1.1 Electron Energy Calibration

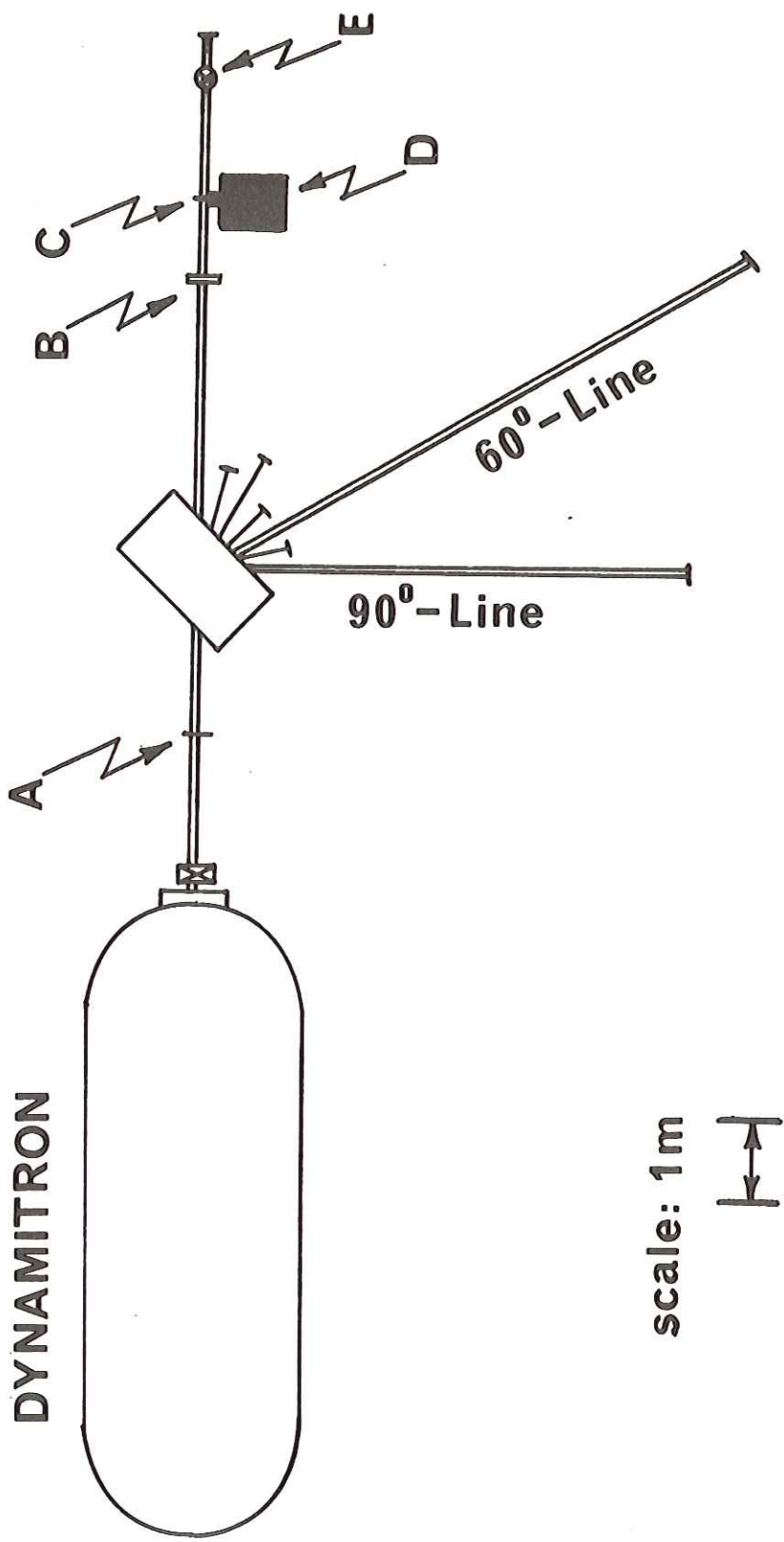
The energy of the electron beam was determined by calibrating the high voltage helipot on the accelerator control console with the electron bremsstrahlung induced ${}^9\text{Be}(\gamma, n)$ reaction which has a threshold of 1666 ± 2 keV (H58). The threshold was determined by detection and measurement of ${}^9\text{Be}$ photoneutrons.

FIGURE 2.1

Physical Arrangement of SUNY/Albany
Dynamitron Accelerator Beam Lines

Legend

- A: permanent 2.54 cm diameter aperture
- B: vacuum gate valve
- C: target position
- D: detector and shielding
- E: vacuum pumping station



Bremsstrahlung was produced by electron irradiation of a 120 mg/cm^2 thick gold foil backed by a 1.27 cm thick high-purity graphite electron stop. A detail of this electron bremsstrahlung radiator assembly is provided in Figure 2.2. The assembly was mounted on a 2" brass blank-off connected to a 4" to 2" beam tube reducer on the end of the beam line (see Figure 2.4, position E). The intensity at the high energy part of the bremsstrahlung distribution is favored with this design since the thin gold foil which produces only a small loss of incident electron energy has a high radiation yield (fraction of electron energy converted into bremsstrahlung energy), while the electron is stopped in the graphite which has a low radiation yield. For example, 2 MeV electrons would lose an average of $\sim 160 \text{ keV}$ with a 0.128 radiation yield on traversing the gold foil, but would lose the remainder of their energy with a radiation yield of 0.0084 in the graphite (BS64). Further details regarding the shape of bremsstrahlung spectra as a function of electron energy, radiator material and thickness can be found in the review by Koch and Motz (KM59).

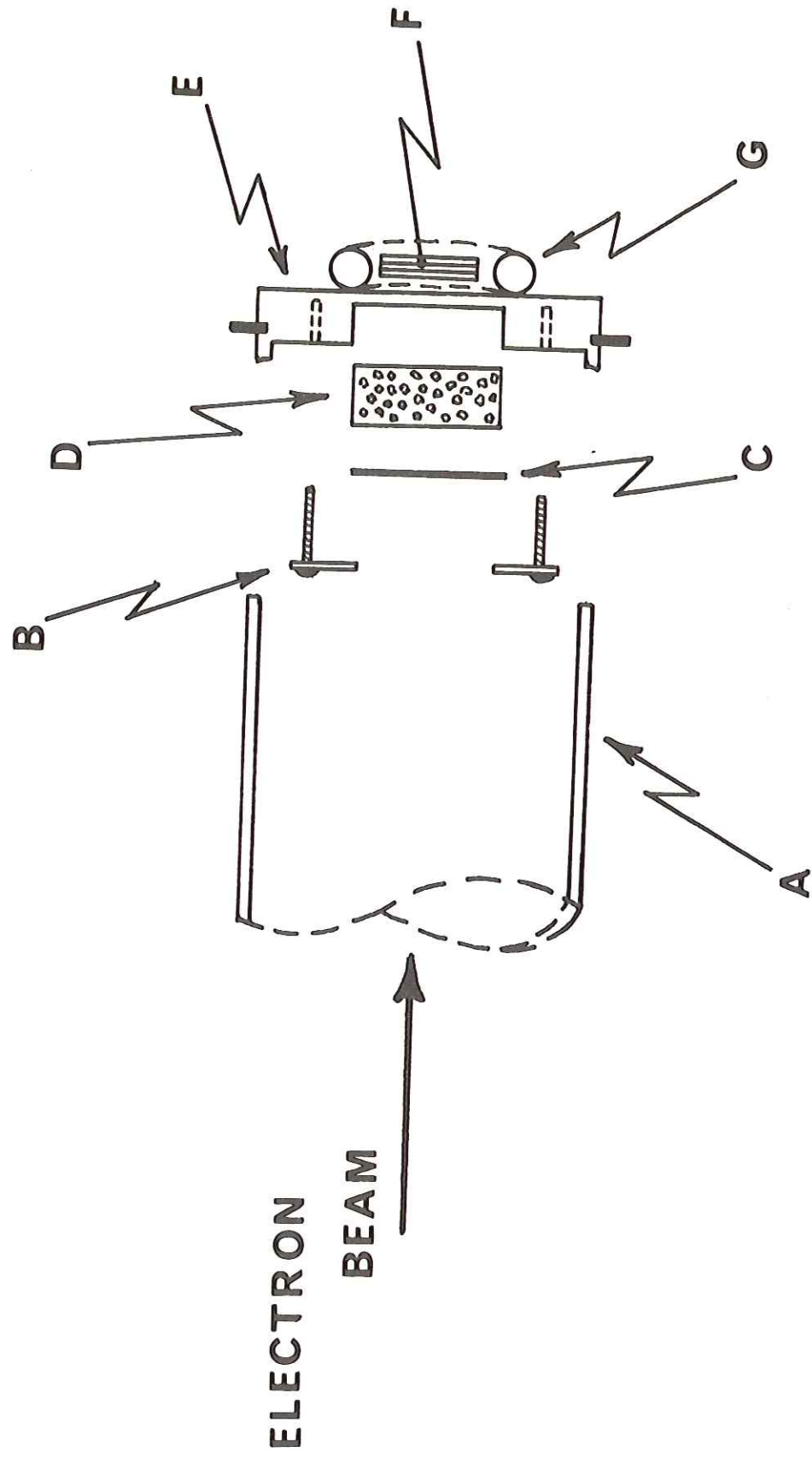
The Be target consisted of a stack of three 40 mil foils with a surface area of $\sim 7 \text{ cm}^2$. As shown in Figure 2.2, it was located directly behind the radiator at the end of the zero-degree beam line (see Figure 2.4, position E).

A ^{10}B -"long" counter located at 90° to the incident electron beam direction at a distance of 30 cm from the Be target was used to detect the neutrons. The operating potential of the long counter was 1500 volts. Pulses from the counter were amplified (Ortec 109A and 451) and counted with a scaler (Ortec 430). Since the maximum or end point

FIGURE 2.2
Electron Bremsstrahlung Radiator Assembly

Legend

- A: end section of 4" to 2" beam tube reducer
- B: aluminum ring plate
- C: gold radiator (120 mg/cm^2)
- D: graphite electron stop (1.27 cm thick)
- E: 2" brass blank-off
- F: stacked Be foils
- G: copper cooling (water) coil



of the bremsstrahlung distribution is characterized by the energy of the incident electrons, the onset of photo-neutrons will occur with an electron beam at the energy of the reaction threshold (1666 ± 2 keV). The neutron yield was measured as a function of the HV-helipot setting, i.e., the energy of the electron beam. The yield at a given helipot setting was normalized to the total charge collected on the bremsstrahlung radiator. By normalizing the yield to the collected charge, the measurements are invariant of the beam current which was typically $1\text{-}5$ μA . The calibration curve of Figure 2.3 was obtained from measurements with total charge collections of either 600 or 2400 μC . The data points shown in the Figure are weighted averages of all measurements made at the same helipot setting. Their error bars (one standard deviation) represent the propagated statistical counting uncertainties in the measurements. As indicated by the inflection in the calibration curve, the threshold (1666 ± 2 keV) occurs at the helipot setting of 2.66 ± 0.01 . Thus, the electron energy for a given helipot setting can be precisely determined. For example, the electron energy corresponding to a setting of 3.250 ± 0.001 is

$$\begin{aligned} E_e &= (1666 \pm 2) \left(\frac{3.250 \pm 0.001}{2.66 \pm 0.01} \right) \\ &= 2036 \pm 8 \text{ keV} \end{aligned}$$

2.1.2 Electron Beam Positioning

A schematic layout of the zero-degree beam line is provided in Figure 2.4. The vacuum gate valve shown in the figure at position A was used to close off the accelerator vacuum when opening the experimental section to air. For reference, this valve is also shown as

FIGURE 2.3

Dynamitron Energy Calibration by ^9Be (γ , n)
Reaction Threshold

Neutron counts from ^{10}B -"long" counter per collected
electron charge (milliCoulomb) as a function of the
electron energy (HV-helipot setting).

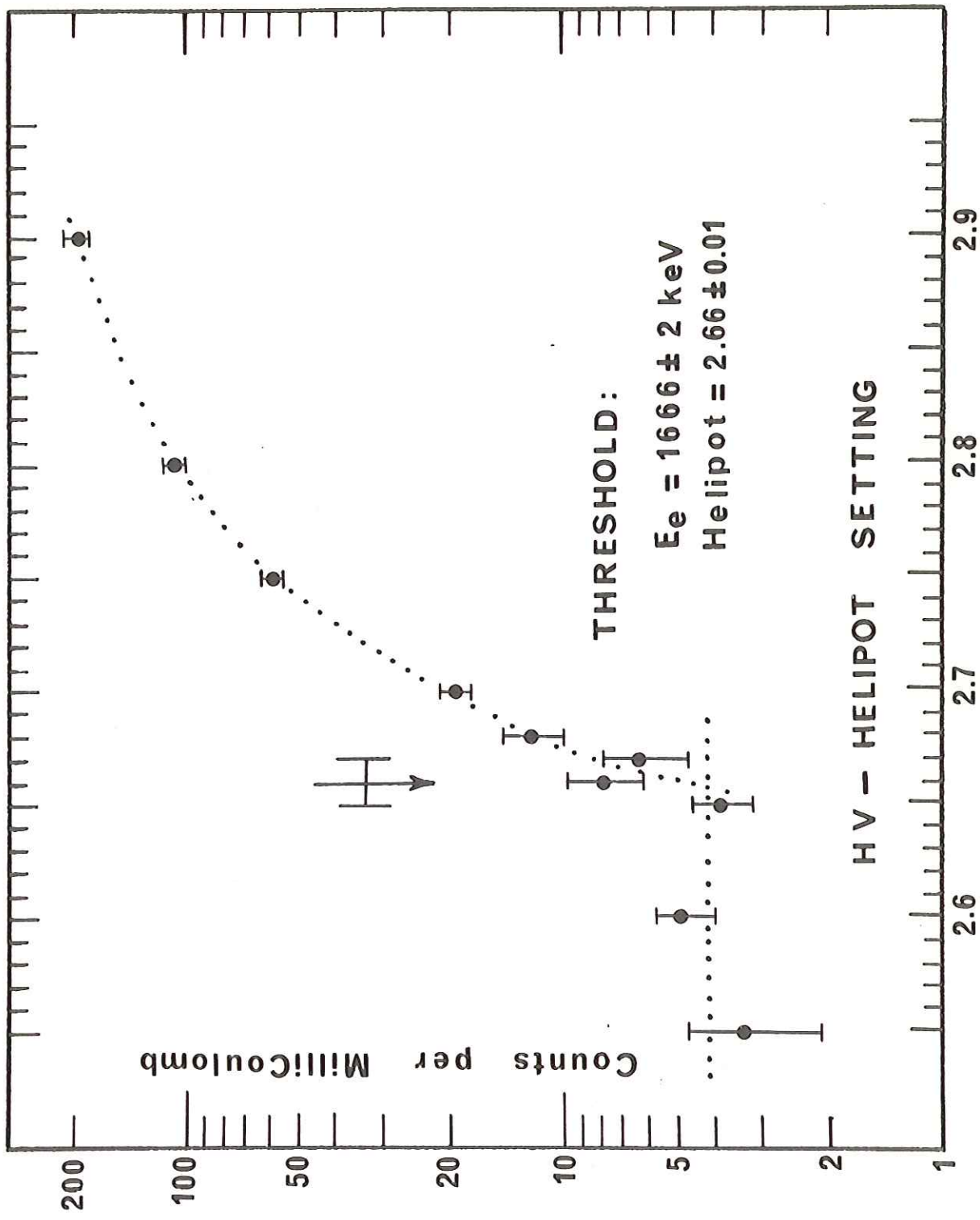
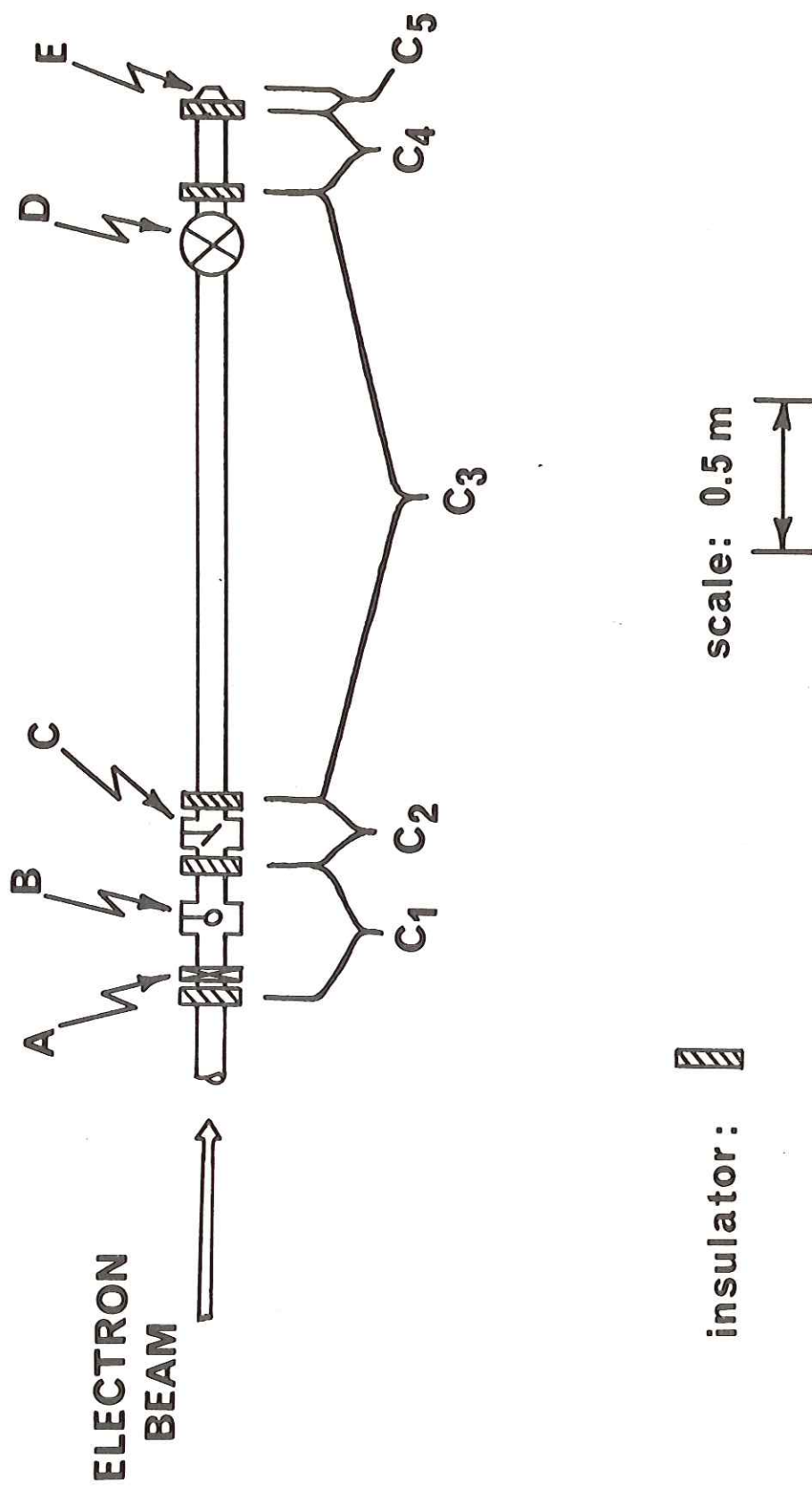


FIGURE 2.4
Dynamitron Zero-Degree Beam Line Sections

Legend

- A: vacuum gate valve
- B: removable 1 cm diameter aperture
- C: target chamber
- D: vacuum pumping station
- E: blank-off (position for bremsstrahlung radiator)



position B in Figure 2.1 and was located at 5.4 m downstream from the permanent 2.54 cm aperture (see Figure 2.1, position A). The beam line extended 304 cm beyond this gate valve. The high-vacuum pumping station (Figure 2.4, position D) was used to evacuate the experimental section before opening it to the accelerator vacuum. This pumping system consisted of a molecular diffusion pump "backed-up" by a mechanical fore-pump which was used to obtain the rough vacuum. With this system it was possible to evacuate the experimental section to $\sim 10^{-5}$ mm Hg from atmospheric pressure in less than 10 minutes.

A schematic of the X-ray target chamber is shown in Figure 2.5. It was located as shown in Figure 2.4 at 30 cm downstream from the removable aperture. The chamber consisted of a 4" beam tube cross and was insulated from the beam line with Neoprene insulators in the bolted vacuum couplings. The aluminum target frame was mounted inside the chamber at 45° to the incident electron beam direction. A detail of the target frame is provided in Figure 2.6. The beam line extended 250 cm beyond the target position and served as both a beam dump and as a connecting link to the pump station. A 1 cm diameter removable aperture located at 24 cm downstream from the gate valve (see Figure 2.4, position B) was used for beam positioning. Figure 2.7 contains a detail of this aperture assembly. It was mounted inside a 4" beam tube cross and had two positions ("in-beam" and "out-beam"). Current measurements could be made on it since it was electrically isolated from the beam tube.

The beam line was electrically isolated into five sections using Neoprene insulators in the bolted vacuum couplings which connected

FIGURE 2.5

Target Chamber Assembly

Legend

- A: 4" beam tube cross
- B: Neoprene insulator in bolted vacuum coupling
- C: aluminum target frame
- D: brass blank-off with aluminum cover plate

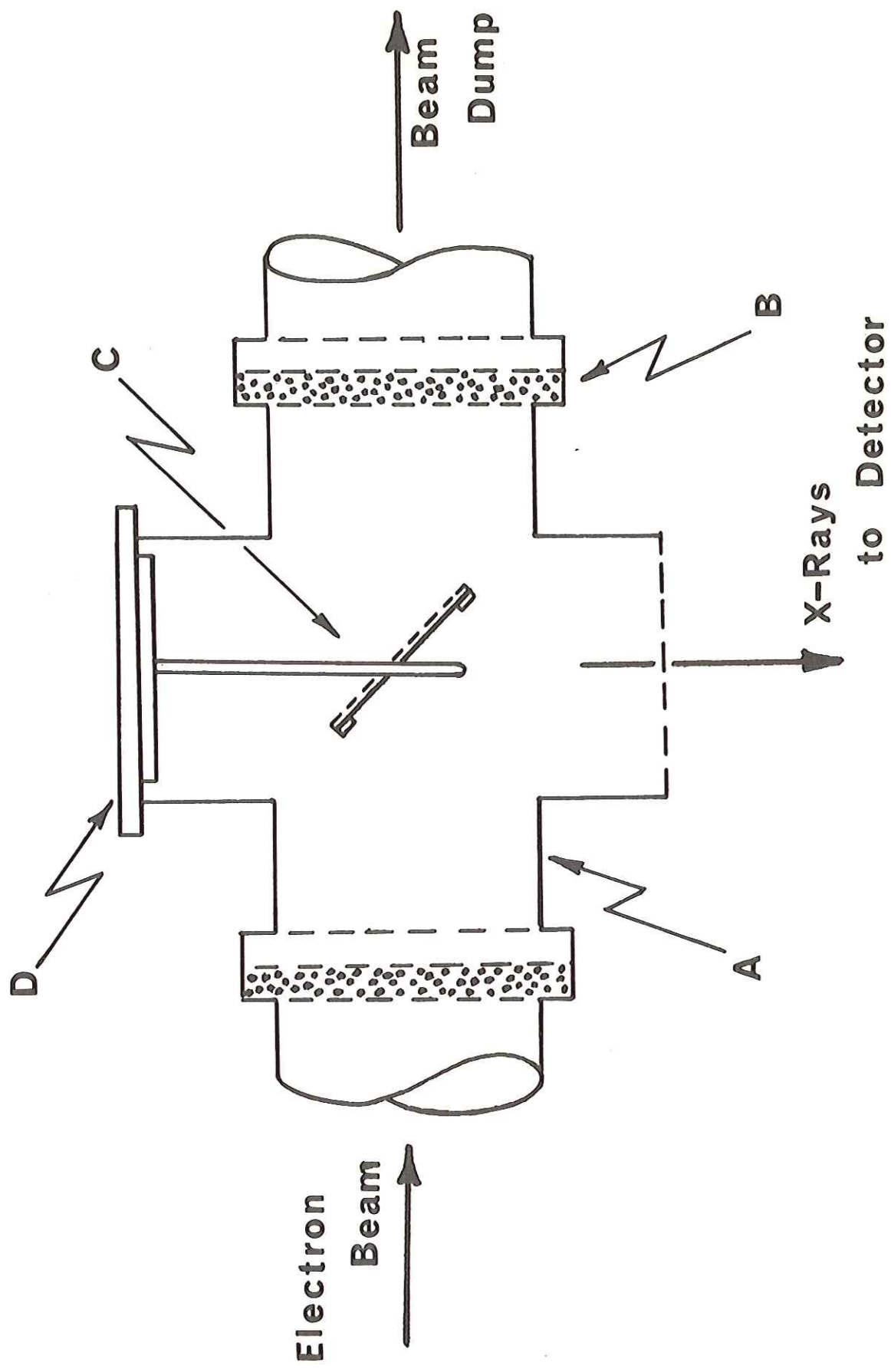


FIGURE 2.6

Aluminum Target Frame Detail

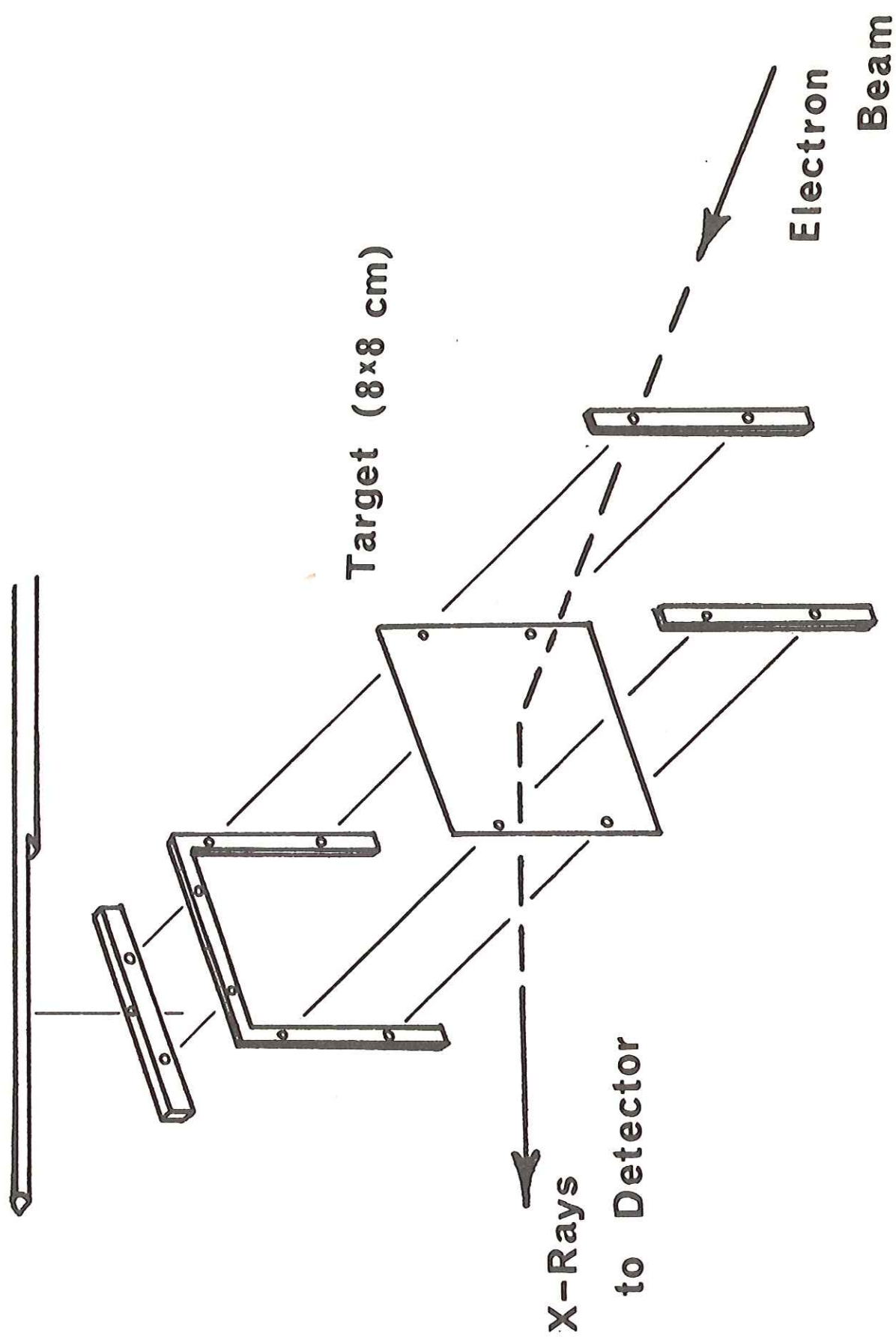
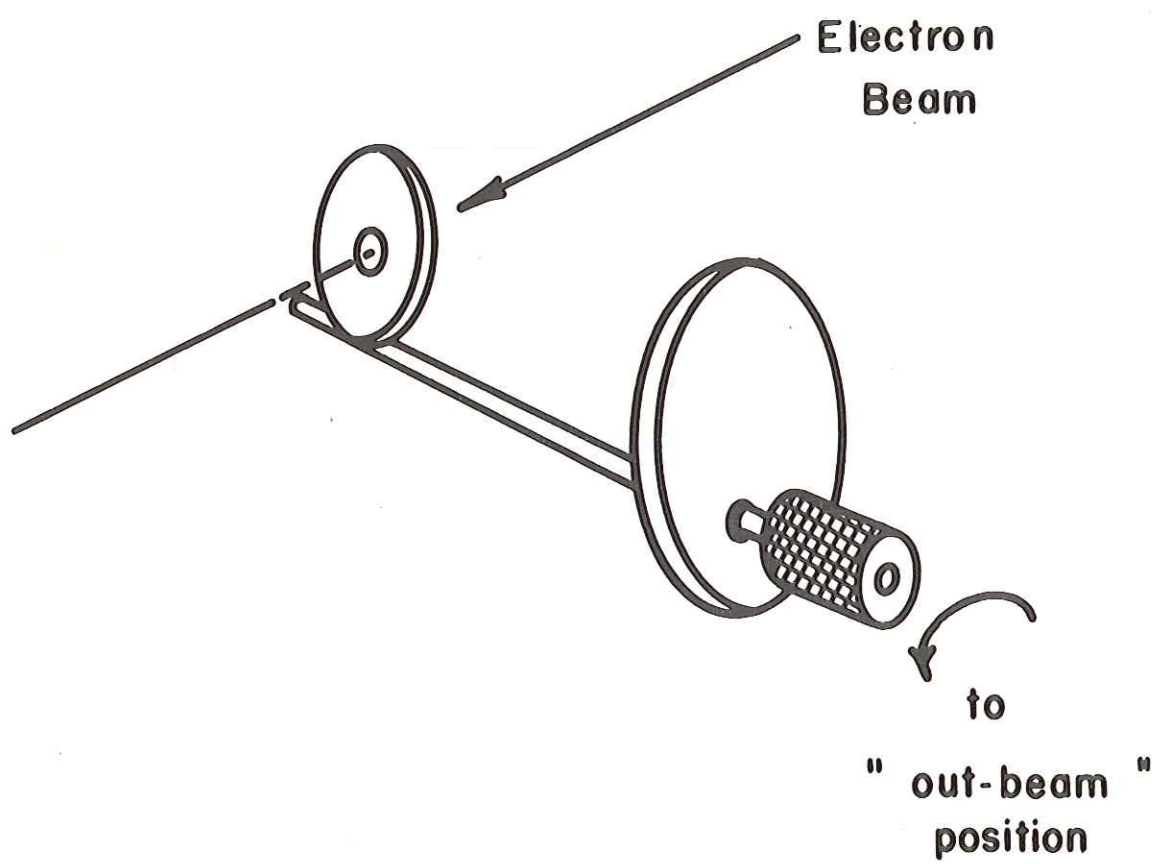


FIGURE 2.7
Removable Aperture Assembly

Shown at "in-beam" position.



the beam pipe sections together. The division of the five sections is shown in Figure 2.4. The electron current on any section could, therefore, be independently monitored. This was extremely convenient for locating and positioning the beam. Beam positioning was effected by trimming and steering the electron beam until the current on the forward sections C_1 and C_2 (see Figure 2.4) and on the removable aperture in the "in-beam" position were minimized. From the relative current measurements on each section, it was possible to insure that the beam was parallel in going through the target chamber and to estimate the beam quality, e.g., the degree of beam scraping. Once the quality of the beam was maximized, its position was further checked by making "burn-spots" on 20 mil polyvinyl chloride sheets mounted on the targets frame at the target position. The "burn-spots" were obtained with 1-2 μA of 2 MeV beam in 1-2 minute irradiations. The beam loading area estimated from the size of the "burn-spots" was $2-3 \text{ cm}^2$. The removable aperture was in the "out-beam" position for the "burn-spots" in order to duplicate the conditions used for the actual X-ray measurements. It was only used for the initial beam positioning since it would produce an undesirable X-ray and bremsstrahlung background in the "in-beam" position.

2.2 Sample and Target Preparations

2.2.1 General Targeting Procedure

The general procedure used to prepare a target for electron irradiation and the subsequent X-ray measurements consisted of immersing a thin adsorbent material into a sample solution, air-drying and mounting on the aluminum target frame. Two types of targets were prepared using either a filter paper or a lens tissue for the adsorbent supporting

matrix. The filter paper used was Whatman No. 541 which is a general ashless quantitative grade filter paper. It has a smooth surface and a thickness of approximately 8.15 mg/cm^2 (0.18 mm). The lens tissue was Fisher No. 11-996 which has a thickness of approximately 1.35 mg/cm^2 . The manufacturer (G72) reported that it is made from 100% bleached long fibre pulp with no further chemical treatment.

Sample solutions were prepared by dissolving a given sample in an appropriate solvent. To insure that the solute deposited on the target is representative of the true or original sample, the entire sample must be soluble in the chosen solvent(s). A description of the various types of samples and the procedures for the solution preparations follow.

2.2.2 Samples, Sample Solutions and Targets

a) References

The samples which were used to determine the relative X-ray yields are referred to as reference samples. One element was chosen to be used as a primary reference in order to measure the relative X-ray yields for any element with respect to the yield of the primary reference. The simultaneous measurement of both yields would, therefore, eliminate the difficulties of trying to normalize independent measurements to each other. It was originally hoped that a large number of the relative yields could be obtained using reference samples of stoichiometric compounds containing the primary reference element. The use of stoichiometric compounds for the reference samples would insure a known atom ratio in the targets. Bromine was initially chosen as the primary

reference since it is nearly in the center of the desired range of elements and as an anion it would chemically combine with many more of the elements. Unfortunately, it was not a very judicious choice since many of the bromine compounds undergo decomposition and are unstable under electron irradiation. These difficulties are described in detail in the Results and Discussion. The second choice for the primary reference element was cadmium. Since cadmium will not combine with elements which are normally cations, reference samples were prepared by weighing out known relative amounts of the element and cadmium. The weights were obtained with a Mettler single pan analytical balance and have an accuracy of about ± 0.2 mg. If the two elements or compounds weighed out do not completely dissolve in the solvent then the atom ratio on the target will be in error. The complete dissolution of the weighed sample in the chosen solvent is the most critical requirement for the target preparation.

Table 2.1 lists the reference sample solutions used for the filter paper targets. For each target, it contains the starting sample reagents, a brief description of the solution preparation, and the final atom ratios. The atom ratios, both with respect to bromine and cadmium, are provided since bromine was used as the primary reference for some of the stoichiometric targets. Typically 10 mmoles of each element were taken for the samples. Although several were made to two different solution concentrations, the majority were made to approximately 0.1 M. The actual solution concentration is not necessary since only the ratio of the number of atoms of each element is important. The solutions prepared with HCl were usually made using a minimum amount of concentrated

Table 2.1
Sample Solutions and Preparation for Filter Paper Targets

Z	Sample	Reagents	Preparation	Z/Br atom ratio*	Z/Cd atom ratio*
19	K/Br	KBrO ₃	dissolve H ₂ O to both 0.5 and 0.1 M	1.0000	-
20	Ca/Cd	CaO, Cd	dissolve HCl, dilute to 0.1 M	-	0.9928
25	Mn/Cd	Mn, Cd	dissolve HCl, dilute to 0.1 M	-	1.0351
26	Fe/Cd	Fe, Cd	dissolve HCl, dilute to 0.1 M	-	1.1001
28	Ni/Br/Cd	NiCl ₂ ·6H ₂ O, CdBr ₂ ·4H ₂ O	dissolve H ₂ O to 0.5 M in Ni	0.5197	1.0394
29	Cu/Cd	Cu, Cd	dissolve HCl, dilute to 0.1 M	-	1.0025
30	Zn/Cd	Zn, Cd	dissolve HCl, dilute to 0.1 M	-	0.8637
35	Br/Cd	CdBr ₂ ·4H ₂ O	dissolve H ₂ O to both 0.5 and 0.1 M in Cd	-	2.0000
37	Rb/Br	RbBr	dissolve H ₂ O to both 0.5 and 0.1 M in Ba	0.5000	-
47	Ag/Cd	AgNO ₃ , Cd(CH ₃ CO ₂) ₂ ·2H ₂ O	dissolve H ₂ O with few drops HNO ₃ , dilute to 0.5 M	-	0.9754
48	Cd/Br	CdBr ₂ ·4H ₂ O	see Br/Cd	0.5000	-
50	Sn/Cd	Sn, Cd	dissolve HCl, dilute to 0.1 M	-	1.0018
56	Ba/Br	BaBr ₂	dissolve H ₂ O to both 0.5 and 0.1 M	1.0000	-

Table 2.1 (cont.)

Sample Solutions and Preparation for Filter Paper Targets

Z	Sample	Reagents	Preparation	Z/Br atom ratio*	Z/Cd atom ratio*
60	Na/Br/Cd	Na ₂ O ₃ , CdBr ₂ ·4H ₂ O	dissolve HCl, dilute to 0.1 M in Na	0.4980	0.9961
62	Sm/Br/Cd	Sm ₂ O ₃ , CdBr ₂ ·4H ₂ O	dissolve HCl, dilute to 0.1 M in Sm	0.4910	0.9821
64	Gd/Br/Cd	Gd ₂ O ₃ , CdBr ₂ ·4H ₂ O	dissolve HCl, dilute to 0.1 M in Gd	0.5594	1.1187
68	Er/Br/Cd	Er ₂ O ₃ , CdBr ₂ ·4H ₂ O	dissolve HCl, dilute to 0.1 M in Er	0.5158	1.0317
70	Yb/Br/Cd	Yb ₂ O ₃ , CdBr ₂ ·4H ₂ O	dissolve HCl, dilute to 0.1 M in Yb	0.5072	1.0145
71	Lu/Br/Cd	Lu ₂ O ₃ , CdBr ₂ ·4H ₂ O	dissolve HCl, dilute to 0.1 M in Lu	0.4474	0.8949
80	Hg/Br	HgBr ₂	dissolve ethanol to both 0.5 and 0.1 M in Hg	0.5000	-
82	Pb/Cd	Pb(CH ₃ CO ₂) ₂ ·3H ₂ O, Cd(CH ₃ CO ₂) ₂ ·2H ₂ O	dissolve H ₂ O to 0.1 M	-	0.9935

*As obtained from direct weighing of the sample reagents. The values do not reflect any uncertainty in the chemical purity of the reagents.

acid and then diluted. If the solutions were too concentrated in acid, the filter paper would decompose and cause it to break up.

Similarly, Table 2.2 contains the reference sample solutions and preparation for the lens tissue targets. Cadmium was used as the primary reference for all the reference samples except for the very light ($Z \leq 20$) elements. Cadmium could not be used with the light elements since its L X-rays would mask the K X-rays from these elements. Copper was used as a secondary reference for the Na, Mg, Al, K and Ca reference solutions. Stoichiometric compounds of $ZnSO_4 \cdot 7H_2O$ and $NiCl_2 \cdot 6H_2O$ were used for the S and Cl samples with Zn and Ni as the secondary references, respectively. Hydrochloric acid could not be used with these light elements either since their X-rays would be masked by the Cl K X-rays. Most of the reference solutions were prepared using ~ 10 mmoles of each element and made to about 0.5 M in an aqueous acidic medium. The atom ratios for all but the heaviest ($Z \geq 60$) elements were around unity. For the heavy elements, the Z/Cd atom ratio was ~ 2 . It was found that the lens tissue was less affected by acids than the filter paper and therefore, much higher acid concentrations could be used in the sample solutions. Because of this, it was even possible to prepare solutions with nitric acid or aqua regia. For example, even concentrated aqua regia only shrunk the lens tissue and did not cause it to break up. This offered a greater flexibility in preparing solutions than was possible for the filter paper targets.

The reagents used for the reference sample solutions were with a few exceptions of reagent grade quality. The reagents which were used are listed by elements in order of increasing atomic number in Table 2.3.

Table 2.2
Sample Solutions and Preparation for Lens Tissue Targets

Z	Sample	Reagents	Preparation	Z/Cd atom ratio*
20	Ca/Cd	$\text{CaCO}_3 \cdot \text{CdCl}_2 \cdot 2\frac{1}{2}\text{H}_2\text{O}$	dissolve HCl, all CO_2 evolved, dilute to 0.5 M	1.0479
23	V/Cd	V, Cd	dissolve aq. regia, expel NO_2 , dilute to 0.25 M	0.9543
24	Cr/Cd	$\text{Cr, CdCl}_2 \cdot 2\frac{1}{2}\text{H}_2\text{O}$	dissolve HCl, dilute to 0.5 M	1.0445
25	Mn/Cd	$\text{Mn, CdCl}_2 \cdot 2\frac{1}{2}\text{H}_2\text{O}$	dissolve HCl, dilute to 0.5 M	0.9673
26	Fe/Cd	$\text{Fe, CdCl}_2 \cdot 2\frac{1}{2}\text{H}_2\text{O}$	dissolve HCl, dilute to 0.5 M	1.0349
27	Co/Cd	$\text{Co, CdCl}_2 \cdot 2\frac{1}{2}\text{H}_2\text{O}$	dissolve HCl, dilute to 0.5 M	0.9624
28	Ni/Cd	$\text{Ni, CdCl}_2 \cdot 2\frac{1}{2}\text{H}_2\text{O}$	dissolve HNO_3 , dilute to 0.5 M	0.9779
29	Cu/Cd	$\text{Cu, CdCl}_2 \cdot 2\frac{1}{2}\text{H}_2\text{O}$	dissolve HCl, dilute to 0.5 M	1.0458
30	Zn/Cd	$\text{Zn, CdCl}_2 \cdot 2\frac{1}{2}\text{H}_2\text{O}$	dissolve HCl, dilute to 0.5 M	1.0025
33	As/Cd	$\text{As}_2\text{O}_3, \text{Cd}$ in As	dissolve HCl, dilute to 0.4 M	2.0146
34	Se/Cd	$\text{SeO}_2, \text{CdCl}_2 \cdot 2\frac{1}{2}\text{H}_2\text{O}$	dissolve H_2O to 0.5 M	0.9675
35	Br/Cd	$\text{CdBr}_2 \cdot 4\text{H}_2\text{O}$	dissolve H_2O to 0.5 M in Cd	2.0000
37	Rb/Br/Cd	$\text{RbBr, CdCl}_2 \cdot 2\frac{1}{2}\text{H}_2\text{O}$	dissolve H_2O to 0.5 M in Rb	0.9993

Table 2.2 (cont..)

Sample Solutions and Preparation for Lens Tissue Targets

Z	Sample	Reagents	Preparation	Z/Cd atom ratio*
38	Sr/Cd	SrCO ₃ , CdCl ₂ ·2H ₂ O	dissolve HCl, all CO ₂ evolved, dilute to 0.5 M	0.9493
47	Ag/Cd	Ag, Cd	dissolve HNO ₃ , dilute to 0.5 M	0.9754
49	In/Cd	In, Cd	dissolve aq. regia, expel NO ₂ , dilute to 0.5 M	0.8048
50	Sn/Cd	Sn, Cd	dissolve HCl, dilute to 0.5 M	0.7761
51	Sb/Cd	Sb, Cd	dissolve aq. regia, expel NO ₂ , dilute to 0.25 M	1.0634
52	Te/Cd	TeO ₂ , Cd	dissolve HCl, dilute to 0.5 M	1.0304
56	Ba/Cd	BaCO ₃ , CdCl ₂ ·2H ₂ O	dissolve H ₂ O to 0.5 M	0.7469
57	La/Cd	La, Cd	dissolve HCl, dilute to 0.1 M	1.0592
58	Ce/Cd	CeO ₂ , Cd	dissolve HNO ₃ , dilute to 0.5 M	0.9026
59	Pr/Cd	Pr ₆ O ₁₁ , Cd	dissolve HCl, dilute to 0.5 M	1.0520
60	Nd/Cd (dup.)	Nd ₂ O ₃ , Cd	dissolve HCl, dilute to 0.5 M in Nd	1.8293 1.9398
62	Sm/Cd	Sm ₂ O ₃ , Cd	dissolve HCl, dilute to 0.5 M in Sm	1.8559

Table 2.2 (cont.)
Sample Solutions and Preparation for Lens Tissue Targets

Z	Sample	Reagents	Preparation	<u>Z/Cd atom ratio*</u>
63	Eu/Cd	Eu ₂ O ₃ , Cd	dissolve HCl, dilute to 0.5 M in Eu	1.5725
64	Gd/Cd (dup.)	Gd ₂ O ₃ , Cd	dissolve HCl, dilute to 0.5 M in Gd	1.9247 1.9099
68	Er/Cd	Er ₂ O ₃ , Cd	dissolve HCl, dilute to 0.5 M in Er	1.9343
70	Yb/Cd	Yb ₂ O ₃ , Cd	dissolve HCl, dilute to 0.5 M in Yb	1.7820
78	Pt/Cd	Pt, Cd	dissolve aq. regia, dilute to 0.25 M	0.9949
80	Hg/Br/Cd	HgBr ₂ , CdBr ₂ ·4H ₂ O	dissolve ethanol to 0.5 M in Hg	1.9048
82	Pb/Cd	Pb, Cd	dissolve HNO ₃ , dilute to 0.5 M in Pb	2.0278
83	Bi/Cd	Bi, Cd	dissolve aq. regia, dilute to 0.5 M in Bi	2.5262
	Z, Z'			<u>Z/Z' atom ratio</u>
11, 29	Na/Cu	NaHCO ₃ , Cu	dissolve HNO ₃ , all CO ₂ evolved, dilute to 0.5 M	1.0227
12, 29	Mg/Cu	Mg, Cu	dissolve HNO ₃ , dilute to 0.2 M	1.1391

Table 2.2 (cont..)

Sample Solutions and Preparation for Lens Tissue Targets

Z, Z'	Sample	Reagents	Preparation	Z/Z' atom ratio*
13, 29	Al/Cu	Al, Cu	dissolve HNO ₃ , dilute to 0.2 M	0.9550
16, 30	S/Zn	ZnSO ₄ ·7H ₂ O	dissolve H ₂ O to 0.5 M	1.0000
17, 28	Cl/Ni	NiCl ₂ ·6H ₂ O	dissolve H ₂ O to 0.5 M in Ni	2.0000
19, 29	K/Cu	KNO ₃ , Cu	dissolve HNO ₃ , dilute to 0.5 M	1.1391
20, 29	Ca/Cu	CaCO ₃ , Cu	dissolve HNO ₃ , dilute to 0.5 M	0.9425
23, 30	V/Zn	V, Zn	dissolve aq. regia, expel NO ₂ , dilute to 0.3 M	0.9625
24, 28	Cr/Ni	Cr, Ni	dissolve HCl, dilute to 0.1 M	1.0056

*As obtained from direct weighing of the sample reagents. The values do not reflect any uncertainty in the chemical purity of the reagents.

Table 2.3
Sample Reagents
(listed by elements in order of increasing atomic number)

NaHCO ₃	Fisher Lot No. 711771, Certified A.C.S.	
	Assay (NaHCO ₃)	99.7%
	Insoluble Matter	0.004%
	Phosphates (PO ₄)	0.0002%
	Sulfur Compounds (as SO ₄)	0.001%
	Ammonium	0.0002%
	Ca, Mg and R ₂ O ₃ ppt.	0.007%
	Heavy Metals (as Pb)	0.0002%
	Iron (Fe)	0.0003%
	Potassium (K)	0.002%
	Chloride (Cl)	0.002%
Mg	MacKay, Certified C.P. Grade, Light Turnings	
Al	Fisher Lot No. 531958, Finest Powder	
KBrO ₃	Eimer and Amend Lot No. 484226, Tested Purity	
	Assay (KBrO ₃)	100.0%
	Bromide (Br)	0.05%
	Heavy Metals (as Pb)	0.0000%
	Insol. Matter	0.000%
	Iron (Fe)	0.0000%
	Nitrogen (N)	0.000%
	Sodium (Na)	0.00%
	Sulfate (SO ₄)	0.000%
KNO ₃	Baker Lot No. 20182, Analyzed Reagent	
	Assay	99.4%
	Insol. Matter	0.003%
	C _l	0.0005%
	IO ₃	< 0.0005%
	NO ₂	< 0.001%
	PO ₄	0.0001%
	SO ₄	0.0005%
	Ca, Mg and R ₂ O ₃ ppt.	0.005%
	Heavy Metals (as Pb)	0.0002%
	Fe	0.0001%
	Na	< 0.020%
CaO	Fisher Lot No. 733520, Certified Reagent, Low in Fluoride	
	Fluoride (F)	0.000%